Structural and Magnetotransport Properties of Nickel/Cobalt Multilayers

James M. Freitag
Centre for the Physics of Materials
Department of Physics
McGill University
Montréal, Québec
Canada

A Thesis submitted to the
Faculty of Graduate Studies and Research
in partial fulfillment of the requirements for the degree of
Master of Science

ISBN 0-612-19812-X

Contents

List of Figures

List of Tables

Abstract

Ferromagnetic/ferromagnetic Ni/Co multilayers with component layer thicknesses ranging from 40 Å down to 5 Å were prepared by DC-magnetron sputtering. The magnetoresistive and soft magnetic properties of Ni-Co alloys are of considerable technological importance in magnetic recording and detection. For this reason, and to study the effect of layering these elements in a modulated structure, the Ni/Co system was chosen. Furthermore, due to the fact that Ni and Co alloys share a common d band, it is expected that the total resistance of the multilayers, including the elemental resistance of the layers and the resistance of the interdiffused alloyed region at the interfaces, will be lower than for other $3d$ transition metal combinations. Consequently, the magnetoresistance ratio $\Delta\rho/\rho$ is expected to be enhanced.

Structural characterization by grazing-angle X-ray reflectivity reveals high-quality layered structures with a well-defined composition modulation along the film growth direction. Quantitative interpretation of the superlattice structure parameters, such as interface roughness, intermixing, and layer thickness fluctuations, has been performed by modelling the X-ray reflectivity data. Wide-angle X-ray diffraction scans display the polycrystalline nature of the Ni/Co multilayers which grow in an FCC phase with a preferred (111) orientation and a fraction of (200) structural domains.

Measurements of the magnetotransport properties of these multilayers indicate that the magnetoresistance (MR) effect, $\Delta\rho \sim 0.35$ $\mu\Omega$-cm, is roughly constant over the entire compositional range. The MR ratio $\Delta\rho/\rho$, which is as high as 3.0% in a Si/(Ni40Å/Co5Å)×6 multilayer, is therefore more strongly dependent on the zero-field resistivity ρ. By fitting a semi-classical model to the resistivity compositional variation, we determined the interface contribution to the resistivity. The MR measurements as well as the magnetic anisotropy of the films, studied by vibrating sample magnetometry (VSM) and magneto-optical Kerr effect (MOKE) magnetometry, are consistent with the origin of the observed MR effect being anisotropic magnetoresistance (AMR). The small magnetic fields required to saturate these multilayers (H_s as small as 40 Oe in some samples) make this system a good candidate for technological applications because of its high magnetic sensitivity. The highest magnetic sensitivity measured at zero-field and constant in the range from ~ -10 Oe to +10 Oe was 0.1%/Oe. This value compares well with other alloys being developed as magnetic sensors.

Résumé

Une série de multicouches ferromagnétique/ferromagnétique Ni/Co fut fabriquée par pulvérisation magnétron continue avec les épaisseurs des couches individuelles qui variaient entre 40 et 5 Å. Les propriétés magnétiques et magnétorésistives des alliages Ni-Co sont importantes du point de vue technologique dans le domaine de l'enregistrement et de la détection magnétique. Pour cette raison, et pour étudier l'effet des interfaces dans la structure stratifiée, le système Ni/Co a été choisi. De plus, puisque les alliages de Ni et Co partagent une bande d commune, la résistivité totale de la multicouche, qui comprend la résistivité des couches individuelles ainsi que la résistivité des régions d'interdiffusion aux interfaces, sera inférieure à celle des autres alliages de métaux de transition $3d$. Conséquemment, le rapport magnétorésistif $\Delta\rho/\rho$ sera augmenté.

Une caractérisation de la structure des échantillons par réflexion de rayons X à angle rasant révèle une structure hétéroépitaxiale de haute qualité avec une modulation de la composition bien définie selon la direction de croissance. Une caractérisation de la structure des multicouches, e.g., la rugosité des interfaces et les fluctations de l'épaisseur des couches, fut effectuée par ajustement d'un modèle théorique de la réflexion des rayons X aux données. Les spectres de diffraction des rayons X à grands angles illustrent la croissance des couches de Ni et Co dans la phase FCC et, en général, mettent en évidence une structure polycristalline avec une orientation préférée (111) et une fraction de domaines (200).

L'étude des propriétés de magnétotransport de ces multicouches indique que l'effet magnétorésistif (MR), $\Delta\rho \sim 0.35$ $\mu\Omega$·cm, est presque constant pour toutes les compositions. Le rapport MR $\Delta\rho/\rho$, s'élevant, dans une multicouche Si/(Ni40Å/Co5Å)×6, jusqu'à 3.0%, dépend donc plus fortement de la résistivité à champ nul ρ. Par ajustement d'un modèle semi-classique à la variation de la résistivité en fonction de la composition, nous avons décelé la contribution des interfaces à la résistivité totale. Les courbes MR et l'anisotropie magnétique des films, étudiée par magnétomètre à échantillon vibrant (VSM) et par magnétomètre à effet Kerr (MOKE), indiquent que la magnétorésistivité anisotropique (AMR) est à l'origine de l'effet MR observé. Les petits champs magnétiques nécessaires à la saturation de ces multicouches (H_s n'excédant pas 40 Oe pour certains échantillons) font de ce système un bon candidat pour des applications technologiques grâce à sa grande sensibilité magnétique. La

plus grande sensibilité mesurée à champ nul et constante sur une région s'étendant de ~ -10 Oe à $+10$ Oe était 0.1%/Oe. Cette valeur se compare avantageusement à celles associées aux autres alliages présentement développés comme senseurs magnétiques.

Acknowledgments

First and foremost, I wish to express my gratitude to my thesis supervisors, Professors Zaven Altounian and John O. Ström-Olsen, for their continued support and guidance throughout my graduate studies at McGill.

I would like to sincerely thank Professor Robert W. Cochrane at l'Université de Montréal for his assistance in the magnetotransport measurements and for useful discussion on thin film magnetism. I also acknowledge the fruitful collaboration with the members of his research group.

I express my special thanks to Dr. Xiaoping Bian who introduced me to the techniques of magnetic multilayer preparation and characterization. In maintaining the sputtering machine, the technical assistance of Frank Van Gils was greatly appreciated.

I wish to thank Professor Mark Sutton for allowing me access to his X-ray diffractometer and for help in the structural analysis. I also thank Professor Peter Grütter for many insightful discussions on surface magnetism and for access to his scanning probe microscopy laboratory.

Finally, I would like to thank all my fellow graduate students for their friendship and help throughout this M.Sc. degree.

1

Introduction

THIS THESIS IS devoted to the study of the structural and magnetotransport properties of Ni/Co multilayers.

A metallic multilayer or superlattice is an artificial structure composed of alternating thin layers of two or more different metals or alloys. Recent advances in the deposition techniques required in the fabrication of these structures, as well as the emergence of sophisticated characterization methods, have spurred much interest into this burgeoning field of scientific research. The new physical properties exhibited by metallic multilayers have attracted so much interest because of the wide range of phenomena associated with very thin films, interfaces, and low-dimensional effects[1, 2, 3, 4, 5, 6]. Active topics of research in multilayers include magnetic surface anisotropy[7], giant magnetoresistance[8] and associated antiferromagnetic coupling of ferromagnetic layers across nonmagnetic spacer layers[9, 10], low-dimensional superconductivity[11], and anomalous mechanical properties[12].

Moreover, the practical application for multilayers are widespread. In fact, thin film deposition is the primary method of fabricating magnetoresistance devices for magnetic recording and the detection of magnetic bubbles. The advantages of thin film technology include the ability to batch-fabricate and to construct magnetic recording head arrays for multi-track use. It offers complete processing on a single chip. From an electrical and magnetic viewpoint, the small volume of the film in such devices leads to high data density and a good electrical impedance match. The refinement of the magnetic structures, upon which these devices are based, to improve the magnetoresistive sensitivity and, consequently, the data storage density potential

is therefore of considerable practical importance. In this context, it has been reported recently that ferromagnetic/ferromagnetic Ni/Co multilayers[13, 14] show large magnetoresistance effects with small saturation fields, leading to high sensitivities which compare well to other current and potential magnetic sensor materials.

1.1 Magnetoresistance Effects in Metals

The phenomenon of magnetoresistance is a galvanomagnetic effect and refers to the change of electrical resistivity of a material due to an external magnetic field. All ferromagnetic and nonmagnetic metals exhibit an increase in electrical resistance as a function of applied field H due to the Lorentz force acting on the conduction electrons[15]. This effect is called the ordinary magnetoresistance (OMR). In general the increase is proportional to H^2, but this can be more complicated both at high magnetic field and low temperature. The effect is appreciable only if the mean free path of the conduction electrons is large compared with the radius of its orbital motion in the magnetic field. The typical magnitude $(\rho(H) - \rho(H = 0))/\rho(H = 0)$ of the OMR in a metal is roughly 10^{-7} in fields $H = 4$ T[16].

Another galvanomagnetic effect, which is purely classical in origin and is exhibited by ferromagnetic metals, is excess resistivity due to the domain structure (ERDS). For the ferromagnetic metals Fe, Ni, Co, and their alloys, the electrical resistance at low temperatures exhibits various anomalies in small fields below ferromagnetic saturation. Most of these anomalies are caused by an internal field $B = \mu_0 M_S$ existing in each magnetic domain. This field acts either through the resistance anisotropy or through the Hall effect generated in the domain. Inversely, an electric current can exert a force on the domain structure and force it to move in the direction of motion of the carriers, causing the "domain drag" effect[17]. If the electron gas applies a dragging force on the domain walls, inversely the walls will exert a reaction force on the electron gas, which manifests itself as the excess resistivity $\Delta\rho$. $\Delta\rho/\rho$ is negative below magnetic saturation. It has been shown that the ERDS effect is not electron scattering by the domain walls, but essentially of electromagnetic

interaction between the magnetic domains and a DC electric current, and is classical in nature[17]. The typical size of ERDS for a ferromagnetic alloy is $\Delta\rho/\rho \approx 10^{-4}$ at room temperature[16].

A further galvanomagnetic phenomenon, anisotropic magnetoresistance (AMR), which will be discussed primarily in this thesis, concerns the variation of resistivity as a function of the direction of magnetization relative to the current. Phenomenologically, the AMR effect is easy to understand. Consider the components of the electric field inside a conductor which are related to the current density through

$$E_i = \sum_j \rho_{ij} J_j, \tag{1.1}$$

where the ρ_{ij} coefficients form the resistivity tensor. Suppose we have a random polycrystal with its magnetization saturated in the z direction. From symmetry arguments[18] one finds that such a magnetized isotropic medium has a resistivity tensor of the form:

$$[\rho_{ij}] = \begin{bmatrix} \rho_\perp(B) & -\rho_H(B) & 0 \\ \rho_H(B) & \rho_\perp(B) & 0 \\ 0 & 0 & \rho_\parallel(B) \end{bmatrix}. \tag{1.2}$$

This form of the resistivity tensor corresponds to the following expression of the electric field **E**:

$$\mathbf{E} = \rho_\perp(B)\mathbf{J} + [\rho_\parallel(B) - \rho_\perp(B)][\alpha \cdot \mathbf{J}]\alpha + \rho_H(B)\alpha \times \mathbf{J}, \tag{1.3}$$

where **J** is the current vector and α is a unit vector in the magnetization (**M**) direction. The ρ_{ij} are functions of the induction B, which depends on the external field H and on the demagnetization factor D of the particular sample geometry. In the cgs system,

$$\mathbf{B} = \mathbf{H} + 4\pi\mathbf{M}(1 - D). \tag{1.4}$$

$\rho_\parallel$ and $\rho_\perp$ are, respectively, the resistivities parallel and perpendicular to α. Starting from an arbitrary resistance characterized by a multidomain configuration, a small *internal* field of 50 Oe or less aligns domains giving $\rho_\parallel$ or $\rho_\perp$. This initial difference $\Delta\rho = \rho_\parallel - \rho_\perp$ is the anisotropic magnetoresistance. The normalized quantity $\Delta\rho/\rho$ is

Table 1.1: Anisotropic magnetoresistance data for selected elements in bulk form.

Element	Temp (K)	ρ_0 ($\mu\Omega$-cm)	$\Delta\rho$ ($\mu\Omega$-cm)	$\Delta\rho/\rho_0$ (%)
Fe	300	9.8	0.02	0.2
	77	0.64	0.002	0.3
Co	300	13.0	0.25	1.9
Ni	300	7.8	0.16	2.0
	77	0.69	0.023	3.3

called the anisotropic magnetoresistivity ratio and is useful for both basic understanding and engineering purposes since it can be obtained directly from $\Delta R/R$ without one needing to know the dimensions of the sample. The last term in Eq. 1.3 gives the extraordinary Hall effect.

The theoretical basis for the AMR effect takes into account the anisotropic scattering mechanism provided by spin-orbit coupling and the splitting of the d-bands in ferromagnetic metals. Whereas the microscopic origin of the effect is believed to be understood, better than order-of-magnitude calculations are not so simple. For example, the fact that $\rho_{\|}$ is nearly always greater than $\rho_{\perp}$ at room temperature is not easily explained. Table 1.1 lists the anisotropic magnetoresistance data for several elements in bulk form, taken from the review article of McGuire and Potter[19]. Figure 1.1 illustrates the anisotropic magnetoresistance ratio for the Ni-Co alloy system. A peak value of $\Delta\rho/\rho \sim 6\%$ around the composition $Ni_{0.8}Co_{0.2}$ is observed; however, the cause of this peak is not well understood. The Ni-Co alloy system is technologically very important due to its large magnetoresistivity and soft magnetic properties. The large MR can be attributed in part to the fact that Ni and Co form a common d-band, thereby reducing the initial resistivity ρ_0 and enhancing the MR ratio $\Delta\rho/\rho_0$. The addition of other $3d$ impurity atoms, such as Cu, Cr, and Mn[20] increases the resistivity of pure Ni to a much greater extent, making Co a better choice for alloys in magnetoresistance applications.

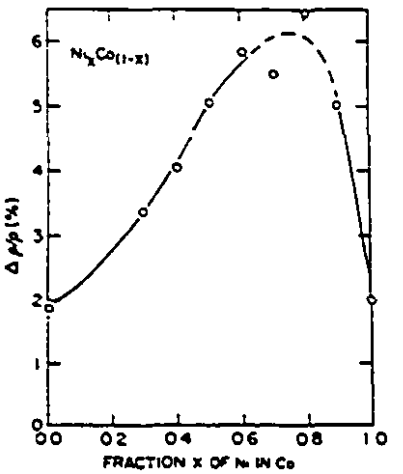

Figure 1.1: Anisotropic magnetoresistivity ratio for $Ni_xCo_{(1-x)}$ alloys (Smit[21] and van Eist[22]).

This thesis presents a study of Ni/Co multilayers. As thin films of these alloys are currently being developed for technological applications, it is of interest to look at how the magnetic and magnetoresistive properties are influenced by the layering of Ni and Co in a modulated structure. In particular, the nature and role of the interfaces between successive layers in the structural and transport properties of the superlattice will be discussed. The structural properties of the Ni/Co multilayers are studied by grazing-angle ($0° < 2\theta < 20°$) and high-angle ($20° < 2\theta < 100°$) diffraction techniques. Quantitative interpretation of the superlattice structure, including interfacial roughness and intermixing, and total surface roughness, is obtained from an analysis of the diffraction data. Magnetic hysteresis and the magnetization process are studied by vibrating sample magnetometry and magneto-optic Kerr effect magnetometry, while transport properties are measured at room temperature in fields up to 1 T.

The thesis is organized as follows: In Chapter 2, the theoretical background of ferromagnetic conductivity and, specifically, the anisotropic magnetoresistance effect is introduced. Chapter 3 explains the experimental methods used for sample preparation and characterization. Finally, Chapter 4 presents the data and analysis of the structural, magnetic, and magnetotransport properties of Ni/Co multilayers, with the conclusions following in Chapter 5.

2

Theoretical Background

THE TRANSPORT PROPERTIES of magnetic metals and alloys, in contrast to other materials, depend on their associated intrinsic magnetization. Microscopically, the conductivity of ferromagnetic $3d$ transition metals is correlated to their distinct electronic structure such as the unfilled d band which is split into spin-up and spin-down components below the ferromagnetic ordering temperature. This chapter presents an overview of conductivity in ferromagnetic metals. In particular, the framework for a semi-classical model of anisotropic magnetoresistance (AMR) is described. Furthermore Appendix A discusses the microscopic origin, spin-orbit coupling, which underlies the AMR effect.

2.1 *Ferromagnetic Metal Conductivity*

Using a quantum mechanical formulation, it is convenient to think in terms of conductivity rather than resistivity, because the basic quantity of interest is the current density J that exists due to an applied force $-e(\mathbf{E} + \mathbf{v} \times \mathbf{B})$ on the electrons. The ith component of J can be written as

$$J_i = \sigma_{ij}(\mathbf{B})E_j = -e \sum_{\textit{all electrons}} v_i = -\frac{e}{8\pi^3} \sum_n \int v_i(\mathbf{k}) f_n(\mathbf{k}) d^3k \qquad (2.1)$$

where $f_n = f_n^0 + g_n$ is the Fermi distribution function for the nth band, written in terms of the equilibrium distribution function f^0 and a small correction g. There are as many f_n in the problem as partially filled bands. These functions are solutions to Boltzmann's equation, which demands that in the steady state the time rate of change of f_n due to the applied force is cancelled by that due to collisions.

In the one-electron picture of metals, each electron moves in the periodic potential of the lattice and the *average* potential of all the other electrons. The solutions to Schrödinger's equation for this potential are stationary states $\psi_{n,\mathbf{k}}$ which, by definition, have infinite lifetime and consequently lead to infinite conductivity. Only deviations from perfect periodicity of the lattice caused by phonons, impurities, grain boundaries, etc., allow an electron initially in the state $|n,\mathbf{k}\rangle$ to be found later in a state $|n',\mathbf{k}'\rangle$. Thus the word "collisions" means any interaction or scattering process that causes transitions from the single-particle states.

The calculation of $\sigma_{ij}(\mathbf{B})$ would be straightforward if the $f_n(\mathbf{k})$ were known. Unfortunately, the $f_n(\mathbf{k})$ are solutions to N coupled nonlinear integro-differential Boltzmann equations ($n = 1, 2, ..., N$) of the form

$$-\frac{e}{\hbar}(\mathbf{E}+\mathbf{v}\times\mathbf{B})\cdot\nabla_{\mathbf{k}}f_n(\mathbf{k}) = \sum_{n',\mathbf{k}'}\{[1-f_n(\mathbf{k})]f_{n'}(\mathbf{k}')P^{n'n}_{\mathbf{k}',\mathbf{k}} - [1-f_{n'}(\mathbf{k}')]f_n(\mathbf{k})P^{nn'}_{\mathbf{k},\mathbf{k}'}\} \quad (2.2)$$

where the sum over states $|n',\mathbf{k}'\rangle$ is such that energy is conserved and where the P's are transition probabilities. In the Born approximation, these probabilities are proportional to the squared modulus of the perturbation potential matrix element connecting initial and final states multiplied by the density of final states. The electronic wavefunctions $\psi_{n,\mathbf{k}}$ needed in order to calculate the transition probabilities

$$P^{n,n'}_{\mathbf{k},\mathbf{k}'} = \frac{1}{4\pi^2\hbar}\frac{|\langle n',\mathbf{k}'|V_{\text{scatt}}|n,\mathbf{k}\rangle|^2}{|\nabla_{\mathbf{k}'}\epsilon(\mathbf{k}')|} \quad (2.3)$$

that appear in Boltzmann's equation must reflect the ferromagnetic ordering of the material.

In the relaxation time approximation[23], the electron experiences a collision in an infinitesimal time interval dt with probability dt/τ. Equation 2.2 can then be rewritten as

$$-\frac{e}{\hbar}(\mathbf{E}+\mathbf{v}\times\mathbf{B})\cdot\nabla_{\mathbf{k}}[f^0_n(\mathbf{k})+g_n(\mathbf{k})] = -\frac{g_n(\mathbf{k})}{\tau_n(\mathbf{k})}. \quad (2.4)$$

The function $g_n(\mathbf{k})$ represents the deviation from equilibrium in the presence of the electric field. The virtue of τ is that in simple cases it turns out to be a function of $|\mathbf{k}|$ instead of $\mathbf{k}$, but at any rate $\tau(\mathbf{k})$ ought to be a simpler function than $f_n(\mathbf{k})$. A

formal series-solution[24] for f_n can be written down in terms of τ:

$$f_n(\mathbf{k}) = f_n^0(\mathbf{k}) + e\frac{\partial f^0}{\partial \epsilon}\{1 + \tau_n(\mathbf{k})\Omega + [\tau_n(\mathbf{k})\Omega]^2 + \cdots\}\tau_n(\mathbf{k})\mathbf{v}\cdot\mathbf{E} \tag{2.5}$$

where Ω is the operator

$$\Omega \equiv \frac{e}{\hbar}(\mathbf{v}\times\mathbf{B})\cdot\nabla_{\mathbf{k}} \tag{2.6}$$

and where it is tacitly assumed the series converges. Substituting this series solution for $f_n(\mathbf{k})$ in terms of $\tau_n(\mathbf{k})$ back into the equation for J_i, Eq. 2.1, gives

$$\sigma_{ij}(B) = \sigma_{ij}^0 + \sigma_{ijk}^1 B_k + \sigma_{ijkl}^2 B_k B_l + \cdots \tag{2.7}$$

where

$$\sigma_{ij}^0 \propto \int \tau \frac{v_i v_j}{|v|} ds \tag{2.8}$$

and where the elements of the higher rank tensors $\sigma_{ijk}^{(1)}$, etc., depend to an increasing degree on the topography of the Fermi surface. In ordinary metals the first term in $\sigma_{ij}(\mathbf{B})$ is the zero-field conductivity and the third term the (ordinary) magnetoresistance effect.

The expression for $\sigma_{ij}^{(0)}$ [Eq. 2.8] indicates that the starting point of the conductivity calculation is to obtain the energy bands $\epsilon_n(\mathbf{k})$ which define the Fermi surface and give the velocity

$$\mathbf{v}_n(\mathbf{k}) = \frac{1}{\hbar}\nabla_{\mathbf{k}}\epsilon(\mathbf{k}) \tag{2.9}$$

associated with each state $|n,\mathbf{k})$. The need for the wavefunctions is subtly disguised in $\tau(\mathbf{k})$.

Figure 2.1 shows a schematic diagram of the density of states for the *sp* and *d* bands in ferromagnetic Ni and Co. The electronic structure of these metals is characterized by the filling of relatively narrow *d* bands capable of holding a total of 10 electrons per atom, leading to a large density of states. The exchange splitting of the *d* bands is given by 2γ as shown in Fig. 2.1. The *d* bands are relatively flat, causing the elements of the effective mass tensor

$$m_{ij}^* = \hbar^2\left[\frac{\partial^2\epsilon(\mathbf{k})}{\partial k_i \partial k_j}\right]^{-1} \tag{2.10}$$

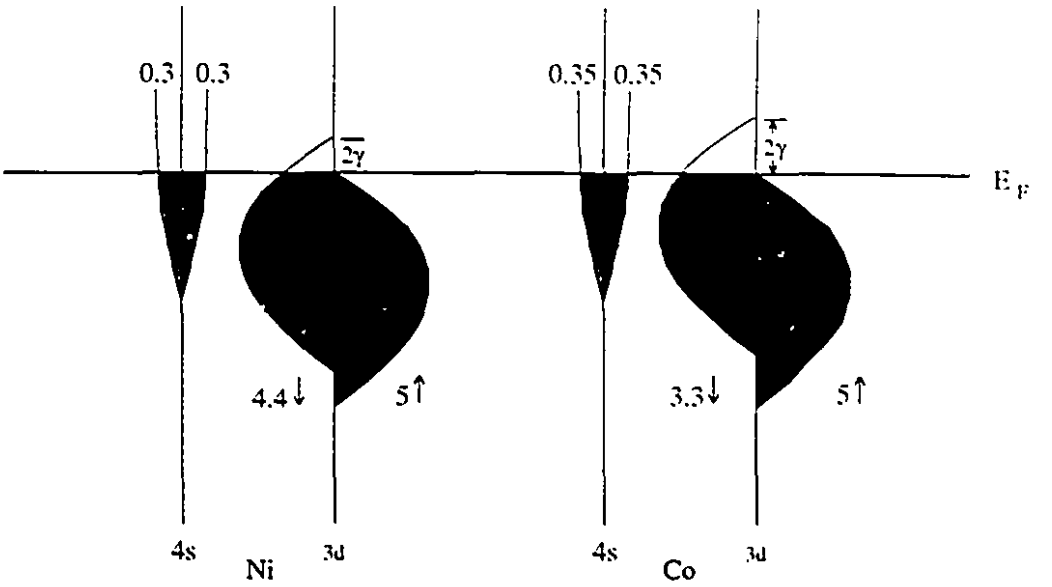

Figure 2.1: Schematic diagram of the density of states in the *sp* and *d* bands of ferromagnetic Ni and Co. The total number of electrons in the down-spin (left) and up-spin (right) bands are also indicated. (After Mathon, Contemp. Phys. 32, 143 (1991).)

to be large. This in turn means that the mobility of d electrons is low. Cutting through and hybridized with the d bands is a broad sp band from the $4s$ atomic level.

Mott [25, 26] first pointed out that in the $3d$ metals, specifically Ni, most of the current is carried by s electrons because m_d^* is large, and that interband (sd) transitions make the dominant contribution to the resistivity because the d density of states at the Fermi level $N_d(\epsilon_F)$ is large. A large m_d^* implies a large $N_d(\epsilon_F)$ if the bands are spherical and parabolic as Mott assumed. This assumption allows him to solve the two coupled Boltzmann equations in the relaxation time approximation, obtaining two constant, isotropic relaxation times τ_s and τ_d. He obtains, approximately,

$$\frac{1}{\tau_s} = \int P^{sd}_{\mathbf{k},\mathbf{k}'} ds' = \frac{\pi}{\hbar} N_d(\epsilon_F) \int \left| V^{sd}_{\mathbf{k},\mathbf{k}'} \right|^2 \sin\theta' d\theta' \tag{2.11}$$

where θ' is the angle between k and k'. The conductivity is simply

$$\sigma = \frac{n_s e^2 \tau_s}{m_s^*} \tag{2.12}$$

where m_s^* is approximately the free electron mass and τ_s is inversely proportional to $N_d(\epsilon_F)$. Mott's model not only explains the relatively high resistivity of Ni, but also

the decrease in resistivity upon ferromagnetic ordering: The d bands split with the majority spin bands entirely below the Fermi level, causing a decrease in $N_d(\epsilon_F)$.

A common simplification is to assume that there are two largely independent conduction channels, sometimes referred to as the "two-current" model, corresponding to the majority ($\uparrow$) and minority ($\downarrow$) sp electrons which independently contribute to the conductivity whenever spin is conserved in the scattering process. This is the case for most scattering potentials that do not depend on spin (e.g., phonons, impurities, etc.) and should be a good approximation at temperatures well below the Curie temperature where the number of magnons is negligible. Thus,

$$\sigma = \sigma_{s\uparrow} + \sigma_{s\downarrow}. \tag{2.13}$$

Another simplification results by assuming that the probabilities of sd scattering and ss scattering are additive, thus

$$\frac{1}{\tau} = \frac{1}{\tau_{ss}} + \frac{1}{\tau_{sd}} \tag{2.14}$$

When combined with the two-current model, this gives

$$\sigma = \frac{ne^2}{m_s}\left[\left(\frac{1}{\tau_{ss}} + \frac{1}{\tau_{s\uparrow d\uparrow}}\right)^{-1} + \left(\frac{1}{\tau_{ss}} + \frac{1}{\tau_{s\downarrow d\downarrow}}\right)^{-1}\right] \tag{2.15}$$

where $n \equiv n_{s\uparrow} = n_{s\downarrow}$ and $\tau_{ss} \equiv \tau_{s\uparrow s\uparrow} = \tau_{s\downarrow s\downarrow}$. It is expected that $\tau_{s\uparrow d\uparrow}$ and $\tau_{s\downarrow d\downarrow}$ will be different because the d band is exchange split.

2.2 *Semi-Classical Model of Anisotropic Magnetoresistance (AMR)*

The starting point for this calculation is the linear response spin-dependent Boltzmann transport equation in the relaxation time approximation [Cf. Eq. 2.4]

$$\mathbf{v}\cdot\frac{\partial g^{\uparrow(\downarrow)}(\mathbf{v},\mathbf{r})}{\partial \mathbf{r}} - e\mathbf{E}\cdot\mathbf{v}\frac{\partial f_0^{\uparrow(\downarrow)}(\epsilon)}{\partial \epsilon} = -\frac{g^{\uparrow(\downarrow)}(\mathbf{v},\mathbf{r})}{\tau^{\uparrow(\downarrow)}} \tag{2.16}$$

where the function $g^{\uparrow(\downarrow)}(\mathbf{v},\mathbf{r})$ represents the deviation from equilibrium in the presence of the electric field $\mathbf{E}$.

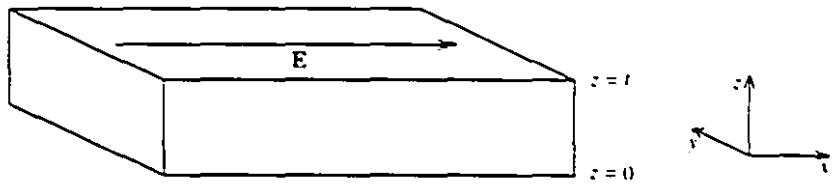

Figure 2.2: Electron transport through a thin film of thickness t, with outer boundaries at $z = 0$ and $z = t$, and electric field E directed along the x axis.

At low temperatures only electrons at the Fermi energy need to be considered. We therefore write $\tau^{\uparrow(\downarrow)} = \lambda^{\uparrow(\downarrow)}/v_F$, in which $\lambda^{\uparrow(\downarrow)}$ is the electron mean free path and the Fermi velocity v_F is assumed to be equal for both spins. The current density follows from integrating the solution for the Boltzmann equation over the velocity space according to

$$\mathbf{J}^{\uparrow(\downarrow)}(\mathbf{r}) = -e\left[\frac{m}{h}\right]^3 \int d^3v \mathbf{v} g^{\uparrow(\downarrow)}(\mathbf{v},\mathbf{r}). \tag{2.17}$$

In order to treat the AMR, we assume a dependence of the mean free path on the angle θ between the electron velocity and the magnetization M. This intrinsically anisotropic mean free path for majority and minority spin electrons is given by

$$\lambda^{\uparrow(\downarrow)}(\theta) = \lambda^{\uparrow(\downarrow)}(1 - a^{\uparrow(\downarrow)}\cos^2\theta - b^{\uparrow(\downarrow)}\cos^4\theta). \tag{2.18}$$

The parameters $a^{\uparrow(\downarrow)}$ and $b^{\uparrow(\downarrow)}$ are a measure for the anisotropy of the scattering, with higher order terms neglected.

We now consider electron transport through a thin film of thickness t, with outer boundaries at $z = 0$ and $z = t$, and electric field E directed along the x axis, as shown in Fig. 2.2. We assume that the scattering at the outer boundaries is purely diffusive, which implies

$$\begin{aligned} g^{\uparrow(\downarrow)}(\hat{\mathbf{v}},0) &= 0, \quad \text{if } \hat{v}_z < 0, \\ g^{\uparrow(\downarrow)}(\hat{\mathbf{v}},t) &= 0, \quad \text{if } \hat{v}_z > 0 \end{aligned} \tag{2.19}$$

where $\hat{v}_z$ is a unit vector in the direction of the z component of velocity. The solution g of Eq. 2.16 can now be written[27]

$$g^{\uparrow(\downarrow)}(\hat{\mathbf{v}},z) = eE\hat{v}_x\left[\frac{\partial f_0(\epsilon)}{\partial \epsilon}\right]\lambda_{\text{eff}}^{\uparrow(\downarrow)}(\hat{\mathbf{v}},z). \tag{2.20}$$

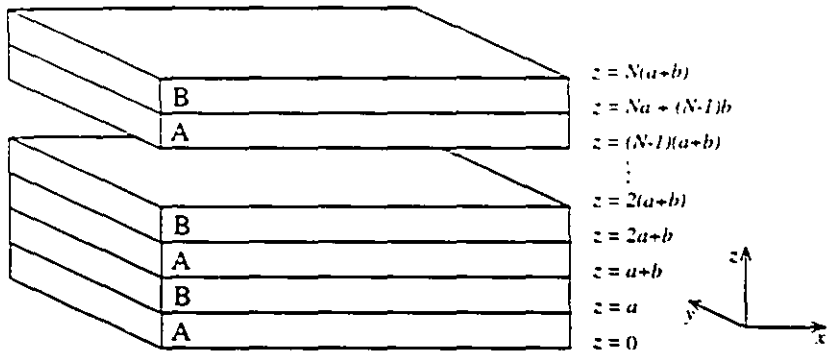

Figure 2.3: Geometry of a magnetic multilayer consisting of magnetic layers A and B of thicknesses a and b, respectively.

By construction, the effective mean free path $\lambda_{\rm eff}^{\Upsilon(\downarrow)}(\hat{\mathbf{v}},z)$ includes bulk scattering as well as scattering at the boundaries:

$$\begin{aligned}\lambda_{\rm eff}^{\Upsilon(\downarrow)}(\hat{\mathbf{v}},z) &= \lambda^{\Upsilon(\downarrow)}(\theta)\left[1-\exp\left[\tfrac{-z}{\lambda^{\Upsilon(\downarrow)}(\theta)\hat{v}_z}\right]\right], \quad \text{if } \hat{v}_z<0,\\ \lambda_{\rm eff}^{\Upsilon(\downarrow)}(\hat{\mathbf{v}},z) &= \lambda^{\Upsilon(\downarrow)}(\theta)\left[1-\exp\left[\tfrac{t-z}{\lambda^{\Upsilon(\downarrow)}(\theta)\hat{v}_z}\right]\right], \quad \text{if } \hat{v}_z>0.\end{aligned} \tag{2.21}$$

Note that this form of $\lambda_{\rm eff}^{\Upsilon(\downarrow)}(\hat{\mathbf{v}},z)$, together with Eq. 2.20, obeys the boundary conditions of Eq. 2.19. The conductivity as a function of the angle between M and E follows from integrating $g^{\Upsilon(\downarrow)}(\hat{\mathbf{v}},z)$, as given by Eq. 2.20, combined with Eqs. 2.18 and 2.21 over a unit sphere in velocity space, using Eq. 2.17, and averaging the resulting current density over the film thickness, yielding

$$\sigma^{\Upsilon(\downarrow)} = \frac{ne^2}{2mv_F}\frac{1}{t}\int_0^t d^3\hat{v}\hat{v}_x^2\lambda_{\rm eff}^{\Upsilon(\downarrow)}(\hat{\mathbf{v}},z). \tag{2.22}$$

Carrying out the integration over z, we obtain

$$\sigma^{\Upsilon(\downarrow)} = \frac{ne^2}{2mv_f}\frac{3}{2\pi}\int_{v_x>0} d^3\hat{v}\hat{v}_x^2\lambda^{\Upsilon(\downarrow)}(\theta)\left\{1-\frac{\lambda^{\Upsilon(\downarrow)}(\theta)\hat{v}_z}{t}\left[1-\exp\left[\frac{-t}{\lambda^{\Upsilon(\downarrow)}(\theta)\hat{v}_z}\right]\right]\right\} \tag{2.23}$$

which is a straightforward extension of the Fuchs-Sondheimer theory[28, 29] of diffuse scattering at surfaces in thin film resistivity.

We now apply this result to a multilayer of the type F_1/F_2 where F_1 and F_2 are two different ferromagnetic layers. Figure 2.3 shows the geometry of such a multilayer with magnetic layers A and B of thicknesses a and b, respectively. For each individual layer, solutions $g_{A,B}^{\Upsilon(\downarrow)}(\mathbf{v},z)$ of the form of Eq. 2.20 are valid. These solutions must be

consequently matched to the appropriate boundary and interfacial conditions:

$$\begin{aligned}
&g_A^{\uparrow(\downarrow)}(\hat{\mathbf{v}},0) = 0, && \text{if } \hat{v}_z < 0,\\
&g_A^{\uparrow(\downarrow)}(\hat{\mathbf{v}},na+(n-1)b) = T^{\uparrow(\downarrow)} g_B^{\uparrow(\downarrow)}(\hat{\mathbf{v}},na+(n-1)b), && \text{if } \hat{v}_z > 0,\\
&g_B^{\uparrow(\downarrow)}(\hat{\mathbf{v}},na+(n-1)b) = T^{\uparrow(\downarrow)} g_A^{\uparrow(\downarrow)}(\hat{\mathbf{v}},na+(n-1)b), && \text{if } \hat{v}_z < 0,\\
&g_B^{\uparrow(\downarrow)}(\hat{\mathbf{v}},n(a+b)) = T^{\uparrow(\downarrow)} g_A^{\uparrow(\downarrow)}(\hat{\mathbf{v}},n(a+b)), && \text{if } \hat{v}_z > 0,\\
&g_A^{\uparrow(\downarrow)}(\hat{\mathbf{v}},n(a+b)) = T^{\uparrow(\downarrow)} g_B^{\uparrow(\downarrow)}(\hat{\mathbf{v}},n(a+b)), && \text{if } \hat{v}_z < 0,\\
&g_B^{\uparrow(\downarrow)}(\hat{\mathbf{v}},N(a+b)) = 0, && \text{if } \hat{v}_z > 0
\end{aligned} \tag{2.24}$$

where $n = 1,2,...,N$ and N is the total number of bilayers (i.e., thickness $t = N(a+b)$). The parameters $T^{\uparrow(\downarrow)}$ determine the probability for an electron to be transmitted through the interface. The functional dependence of the coefficients can be determined by matching the free-electron-like (plane-wave) functions and their derivatives at each interface[30, 31].

The conductivity of these multilayers, as a function of the orientation of the magnetization, is calculated similar to the thin film case [Eq. 2.22], but now averaging over the total thickness of the multilayer, in each region of the multilayer using the appropriate expressions for $g^{\uparrow(\downarrow)}(\hat{\mathbf{v}},z)$, Eq. 2.24. Equation 2.23, together with these boundary conditions, will form the basis of our analysis of the resistivity and magnetoresistance in this study of Ni/Co multilayers.

3

Experimental Methods

THE PREPARATION OF high-quality artificially inhomogeneous superlattices is essential for the purposes of this research. The magnetic multilayers studied were grown in a computer controlled multifunction magnetron sputter deposition system. Details of this system as well as sample preparation methods are described in the first section below.

Ex-situ structural characterization of the integrity of the crystalline layers, interfacial roughness, and the superlattice coherence of the layered structure were obtained by means of high-angle X-ray diffraction and small-angle X-ray reflectivity measurements. A vibrating sample magnetometer (VSM) and a magneto-optical Kerr effect (MOKE) magnetometer were used to measure the magnetic properties of the films. Magnetotransport measurements were performed on a high-resolution ac-bridge in external magnetic fields up to 1 Tesla.

3.1 Sputter Deposition

Magnetic thin films and multilayers can be grown using a wide variety of deposition methods, including electrochemical[32] and vacuum deposition techniques[33, 34, 35]. The latter is subdivided into two main categories: vapor deposition by thermal cell evaporation or electron beam evaporation, a process referred to as molecular beam epitaxy (MBE); and sputtering techniques such as diode, triode, planar magnetron, and ion beam, which are the most effective methods of growing metallic thin films and multilayers. Conventional evaporation is a low-energy process with the kinetic energy of the evaporated source materials typically in the range of 1×10^{-2} to 1 eV[36].

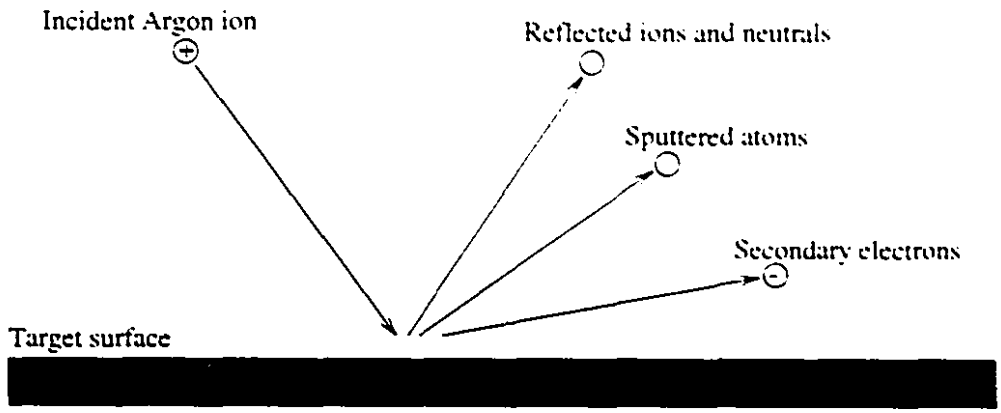

Figure 3.1: Schematic representation of the sputtering process of a positive Ar ion impacting with the target surface.

The nature of this process carries several drawbacks. Foremost, when the evaporated atoms impinge on the surface of the substrate, they diffuse sideways which can cause pin holes to be formed, particularly for films less than 10 nm thick or when a large surface defect is present. Since the films are deposited at low-energy, they may also have poor surface adhesion. Furthermore, the composition of alloy films may differ considerably from the original composition of the target.

In contrast, sputter deposition uses high-energy inert particles to knock of atoms from the target material, which are subsequently deposited onto the substrate by bombardment. As illustrated in Fig. 3.1, high-energy particles are created by ionizing an inert sputtering gas such as argon and accelerating them onto the target material surface. This process knocks off target atoms that have typical energies of 2-30 eV[36]. Reflected ions or reflected neutral argon atoms and secondary electrons are also a by-product of the initial process. The energy of the sputtered atoms is reduced prior to deposition at the substrate by collisions with the sputtering gas. The deposition rates obtained will depend on numerous factors, including the target material, accelerating voltage ($\sim$ 500 V), sputtering gas pressure ($\sim$ 1 - 100 mTorr), and the target to substrate distance ($\sim$ 5 - 20 cm). Since nucleation on the substrate occurs at several different sites and there is little diffusion, surface adhesion depends mainly on substrate roughness and cleanness. Figure 3.2 compares the energy distribution of atoms arriving at the substrate for typical thermal evaporation conditions

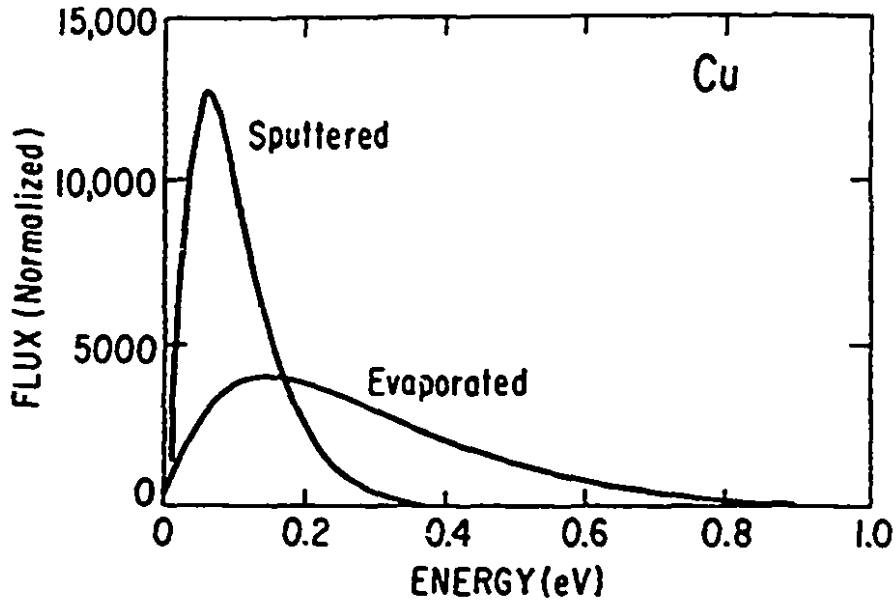

Figure 3.2: Comparison of energy distribution of particle flux arriving at a substrate for sputtering at a pressure of 10 mT and substrate-target distance of 6 cm, and for thermal evaporation[37].

and the sputtering conditions described in the caption[37]. It is seen under these conditions of high sputtering pressure and large substrate-target distance, that the evaporated atoms exhibit a much larger high-energy tail and are centered at higher energies than the sputtered atoms, implying that sputtering is less damaging than thermal evaporation with, nevertheless, comparable deposition rates. Sputter deposition is therefore a relatively simple and inexpensive method of growing high-quality metallic films. Its principal advantages include the high deposition rates obtained for most materials, and the fact that alloys or compounds can be used as targets.

A magnetron sputtering system is designed with permanent magnets around the target that produce a magnetic field to confine the plasma close to the target and away from the substrate. This reduces damage to the substrate and film due to ion bombardment and allows lower sputtering pressures with no commensurate decrease in deposition rate. Furthermore, magnetron sputter deposition leads to films with comparatively low gas impurity levels. In fact, the concentration of impurities in the deposited films from residual gases, such as oxygen and nitrogen, depend on the film growth rate and the residual gas pressures in the system during deposition.

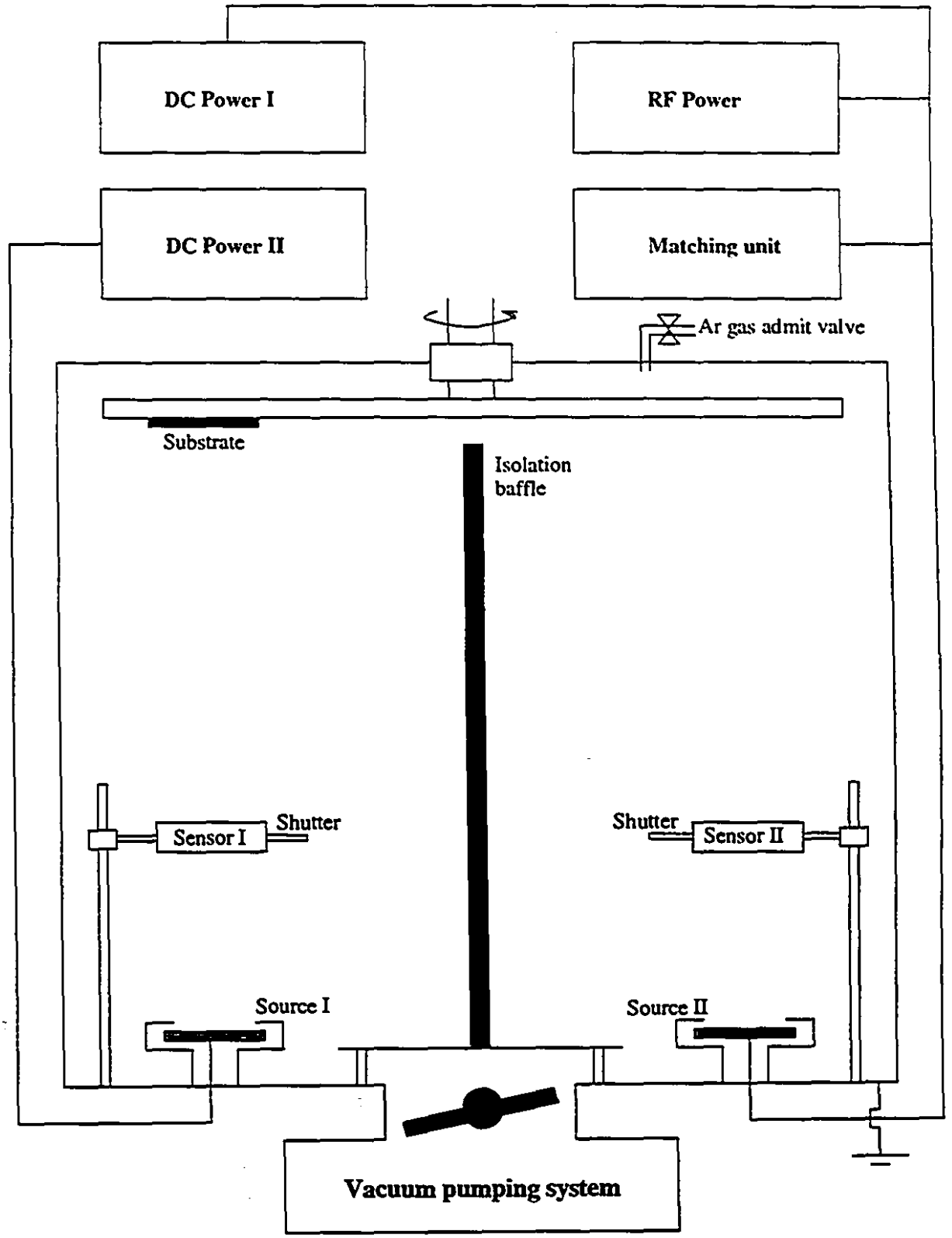

Figure 3.3: A schematic drawing of the multifunction magnetron sputtering system.

Table 3.1: Deposition conditions for the Ni/Co multilayer series. Purity refers to the elemental purity of the targets, P_{argon} is the sputtering pressure of argon gas, P_{DC} is the DC power, D_{st} is the substrate-target distance and τ is the deposition rate for each target.

Target	Purity	$D_{st}(cm)$	$P_{argon}(mTorr)$	$P_{DC}(W)$	τ (Å/s)
Ni	99.98%	14.0	8.0	80	1.32
Co	99.9%	14.0	8.0	80	2.08

In this study, a series of Ni/Co multilayers were grown in an Edwards multifunction deposition system, as shown schematically in Fig. 3.3. The system includes three magnetron sputtering sources that can be operated in either DC or RF modes. In addition, an electron-beam evaporation source is available for the growth of rare-earth buffer or capping layers. A cryo-pump enables base pressures in the vacuum system, prior to deposition, of 2×10^{-7} Torr. The pumping and pressure monitoring procedures are automatically controlled by a microcomputer. The different metallic targets were separated by an isolation shield, and each was isolated from the substrate by a two-position rotating shutter. The deposition rates of individual targets were measured by means of a quartz-crystal thickness monitor. More precise rate calibrations were obtained by low-angle X-ray reflectivity measurements on single film samples. In all subsequent depositions, individual layer thicknesses in the multilayer samples were regulated by computer control of the exposure time and substrate position via a rotating plate on which the substrate is mounted. Furthermore, an internal radiative heater can heat the substrate to a temperature of $\approx$ 300°C. With a typical target-substrate distance of 14 cm, the uniformity of the deposition from the 1.5 inch diameter target used in this system is 5% or better over a distance of 4 cm from the center of the target (see Fig. 3.4)[38].

Table 3.1 describes the deposition conditions for the Ni/Co multilayer series. To clean-up the surface of the targets, a pre-sputtering for a period of several minutes was performed prior to deposition. Multilayered films were then deposited onto either chemically degreased 2 cm^2 oxidized Si(100) wafers through a mask that defined the

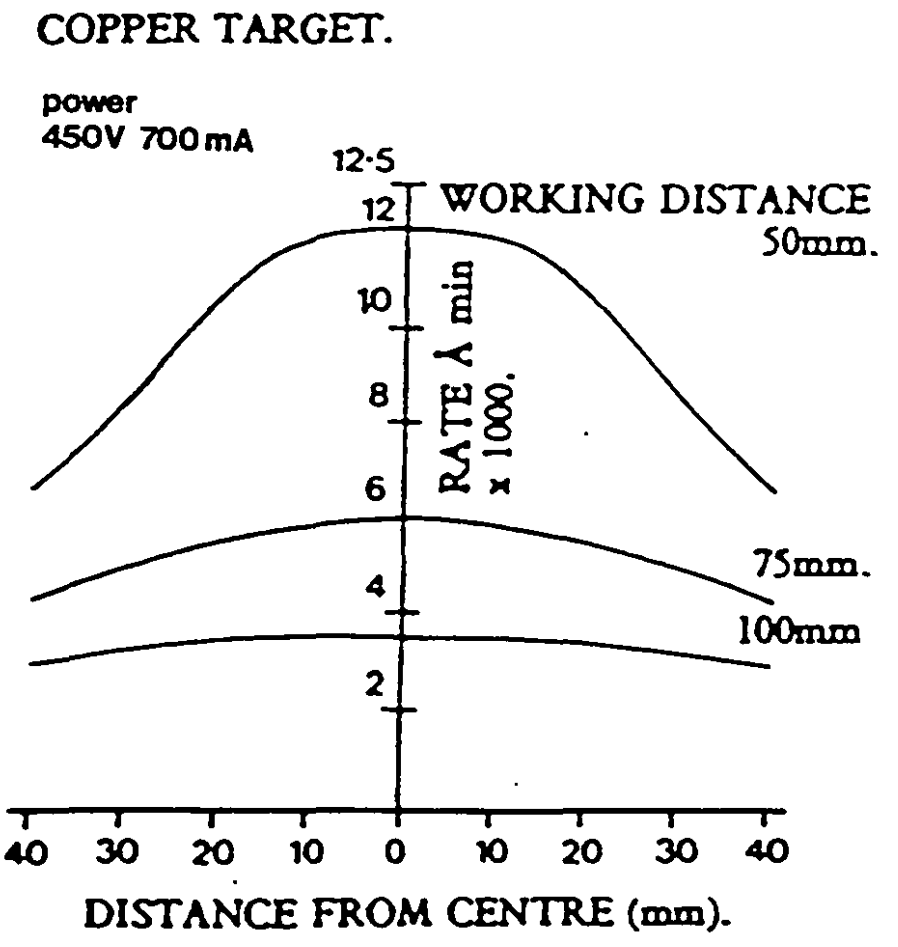

Figure 3.4: Uniformity of magnetron sputter deposition.

sample dimensions appropriate for transport measurements (see section 3.4).

3.2 *X-ray Diffraction*

X-ray diffraction is a non-destructive, fast and reliable method of extracting valuable quantitative information on the crystal structure, morphology, and chemistry of the constituent layers in a superlattice. The most commonly used scattering geometry is reflectivity measurements, in which the scattering vector is along the growth direction of the layers and perpendicular to the film plane. By convention, these measurements are separated into small-angle ($q < 2$ Å^{-1}) and high-angle ($q > 2$ Å^{-1}) regions of the spectrum. In the small-angle region, the length scales probed are much larger than the atomic spacings, so that the scattering can be considered to arise solely

from the chemical modulation of the multilayer structure. For high-angle scattering, information on the crystal structure and the superlattice coherence can be measured. A quantitative analysis by modelling the specular and diffuse components of the reflectivity spectra provides rich information.

3.2.1 *Grazing Angle X-ray Reflectivity*

Small-angle X-ray reflectivity measurements were performed on a high-resolution, triple-axis four circle diffractometer with a conventional 2.2 kW Cu-target tube source. Figure 3.5 shows the major parts of this diffractometer. Three slits with mechanical resolution of 0.01 mm in both the vertical and horizontal directions are placed along the path of the X-ray beam to adjust its cross-section and intensity. In this setup, the source beam of dimension 1×4 mm^2 was reduced by slit 3 to 0.4×2.0 mm^2, and the detector was adjusted to accept all elastically scattered X-ray photons passing through the analyzer housing window (a fourth slit, in essence) and reflected by the analyzer crystal. Two identical Ge single crystals with (111) orientation are used as monochromator and analyzer and provide a resolution of $\sim 0.01°$, full width at half-maximum (FWHM), for a $\theta - 2\theta$ scan, which, using Cu-$K\alpha_1$ radiation, corresponds to a Δq of 0.0014 Å^{-1} in reciprocal space. The sample is mounted on a goniometer with four circles of 2θ, θ, χ, and ϕ, as shown in the inset of Fig. 3.5. In mounting the samples, particular care was taken to maintain the same initial alignment, since the X-ray reflectivity data is very sensitive to this factor. The mounting procedure for each sample was to block half the X-ray beam at $\theta = 0°$, then to perform several θ optimizing scans, as well as ω scans, and a quick $\theta - 2\theta$ longitudinal scan. All measurements were made in a 2θ range between 0.3° and 9° (q = 0.0427 - 1.2757 Å^{-1}) with a step of 0.02° (Δq = 0.0028 Å^{-1}). A typical count rate at the first superlattice peak of $\sim$ 500 cps was measured.

3.2.2 *High-Angle X-ray Diffraction*

High-angle X-ray diffraction experiments were performed on an automated Nicolet-Stöe L11 powder diffractometer using Cu-$K\alpha$ radiation. The system, as illustrated in

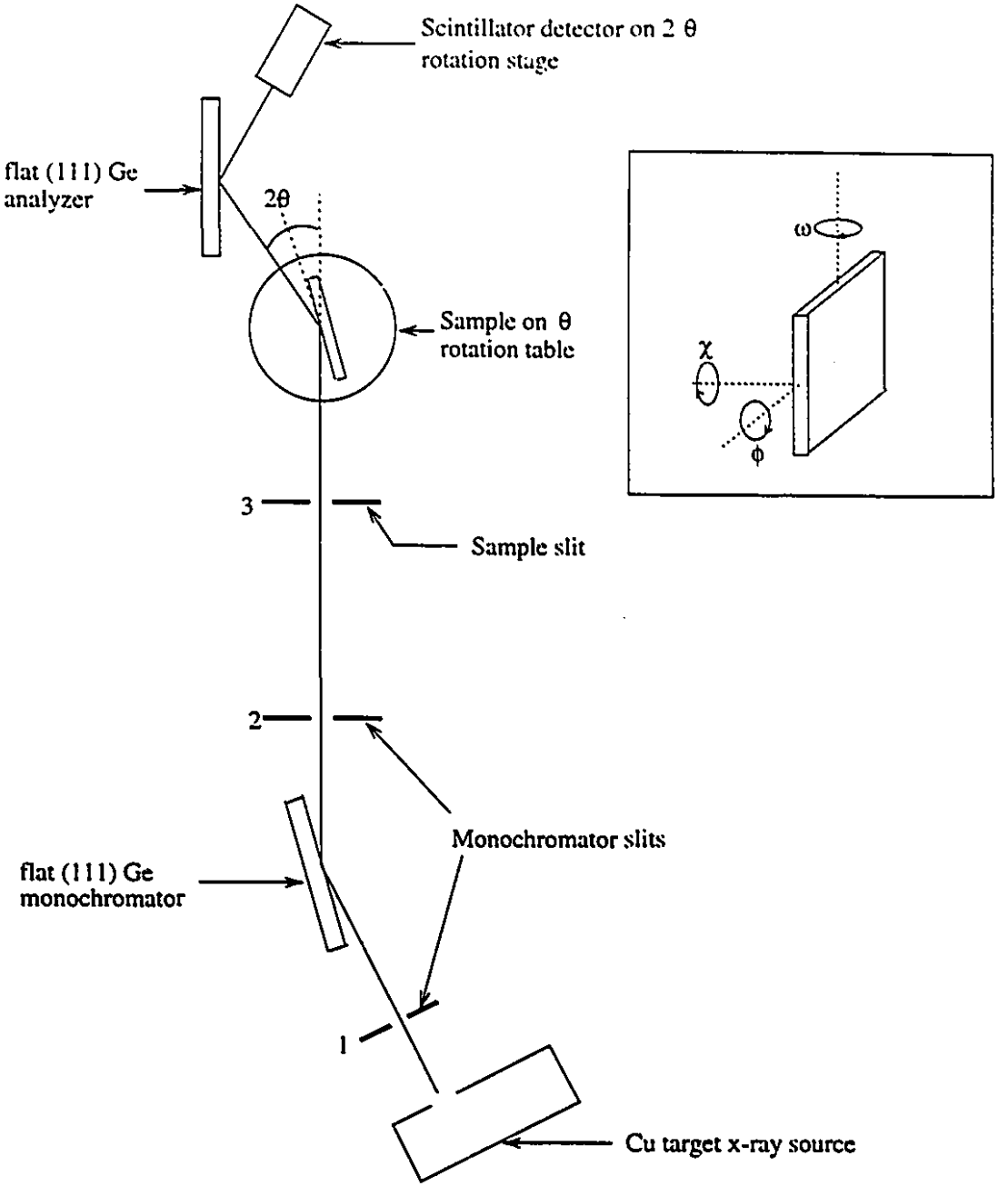

Figure 3.5: Schematic drawing of the high-resolution X-ray diffractometer used for grazing-angle X-ray reflectivity measurements. The inset shows the three rotation axes of the goniometer.

Fig. 3.6, consists of a 2.2 kW Cu-target tube source and a detector with a graphite analyzer. The width of the source slit is 1.8 mm, the detector slit is 0.2 mm and the angular acceptance of the detector is $\sim 0.3°$. With the axial divergence of the beam limited to $\sim 3°$, the instrumental broadening for this diffractometer, as estimated by Al powder diffraction measurements, is 0.15°, FWHM, for a $\theta - 2\theta$ scan. Most measurements were made in the 2θ range between 20° and 100° ($q \sim 1.40 - 6.25$ Å^{-1}) using a step of 0.5° ($\Delta q = 0.04$ Å^{-1}).

3.3 Magnetic Measurements

Magnetometry is the technique generally used to obtain important information about the magnetization, anisotropy, and magnetic phase transition. Additionally, the hysteresis loop provides information on the remanent magnetization, saturation and coercive fields. The methods of measuring magnetic moments can be divided largely into three classes: measurement of a force on a material in a non-uniform magnetic field, measurement of magnetic induction in the vicinity of a sample, and indirect measurements of phenomena which involve the magnetic properties. In this research, the magnetic properties of the soft magnetic Ni/Co multilayers were studied using a technique from each of the two latter classes described above: vibrating sample magnetometry (VSM), and magneto-optic Kerr effect (MOKE, or SMOKE to emphasize the surface nature of the effect). Both methods are fast, reliable and highly-sensitive.

3.3.1 Vibrating Sample Magnetometry

All magnetic induction measurements involve observation of the voltage induced in a detection coil by a flux change when the applied magnetic field, coil position, or sample position is changed. This last method is by far the most successful in its incarnation as the Foner vibrating sample magnetometer (VSM)[39]. At its inception, the novel features of this magnetometer were: sample motion perpendicular to the applied field producing an oscillating dipole field, and a detection coil configuration with effective area-turns nonsymmetrically distributed about the axis of vibration which permits

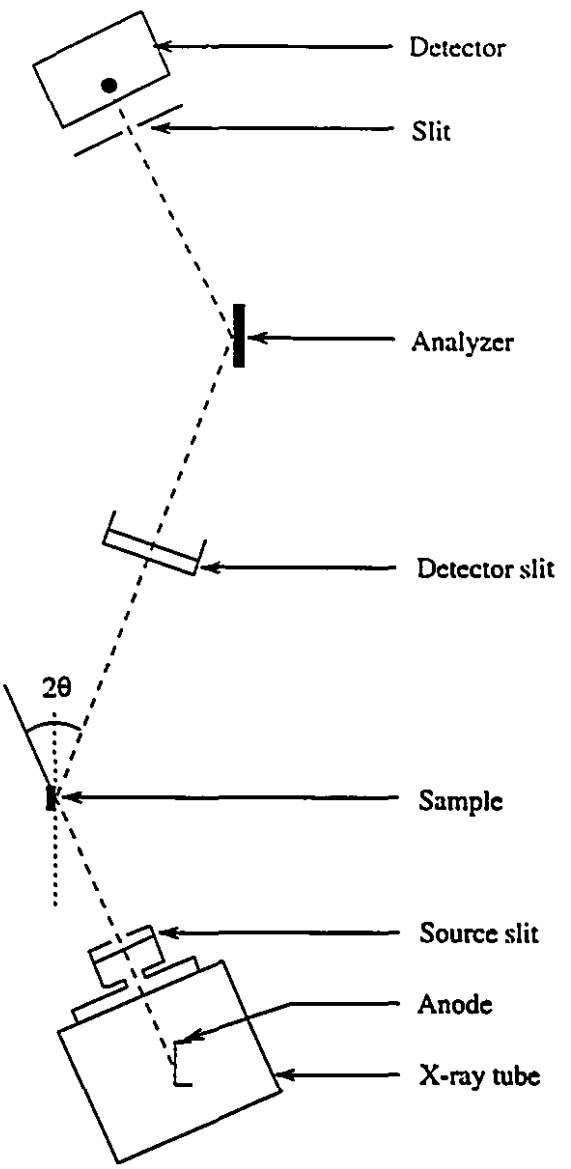

Figure 3.6: Schematic drawing of the high-angle X-ray diffractometer.

the observation of this dipole field. The basic instrument is shown schematically in Fig 3.7. For a sample with moment M_s, the total flux ϕ through the detection coils can be written:

$$\phi = AH + B(4\pi - D)M_s \sin \omega t) \tag{3.1}$$

where A and B are geometrical factors depending on coil geometry, D is the demagnetization factor of the sample, and ω is the vibrating frequency. Hence the emf $\epsilon(= d\phi/dt)$ measured by the coils is:

$$\epsilon = C(4\pi - D)M_s \omega \cos \omega t \tag{3.2}$$

where C is a constant. The amplitude of this emf is measured by a lock-in amplifier circuit. The constant C can be determined by calibration of the instrument using a standard with a known moment. For an external field applied in the plane of the film, the demagnetization factor D is negligible in thin film samples.

The VSM used in this work was a modified Princeton Instruments model 155. The loudspeaker transducer is vibrated by the internal oscillator of the SR830 DSP lock-in amplifier at a frequency of 82 Hz with the induced emf on the pick-up coils synchronously detected by the same instrument. The field magnet is powered by a stable bi-polar power source producing fields up to 200 Oe, which is sufficient to saturate the soft magnetic films studied here. The sample is attached to a plastic sample holder rod with vacuum grease and the entire sample holder can be rotated so that the sample may be placed at any angle with respect to the applied field (in the plane of the film, for all measurements).

3.3.2 *Magneto-Optic Kerr Effect Magnetometry*

The influence of magnetization of a ferromagnetic mirror upon reflected electromagnetic radiation is called the magneto-optic Kerr effect. Phenomenologically, the effect causes linearly polarized incident light to acquire a rotation of the plane of polarization and a consequent ellipticity after reflection from the surface of a magnetized medium. Figure 3.8 illustrates the magneto-optic effect of inducing an orthogonal component in the electric field vector of the reflected light. The component of the

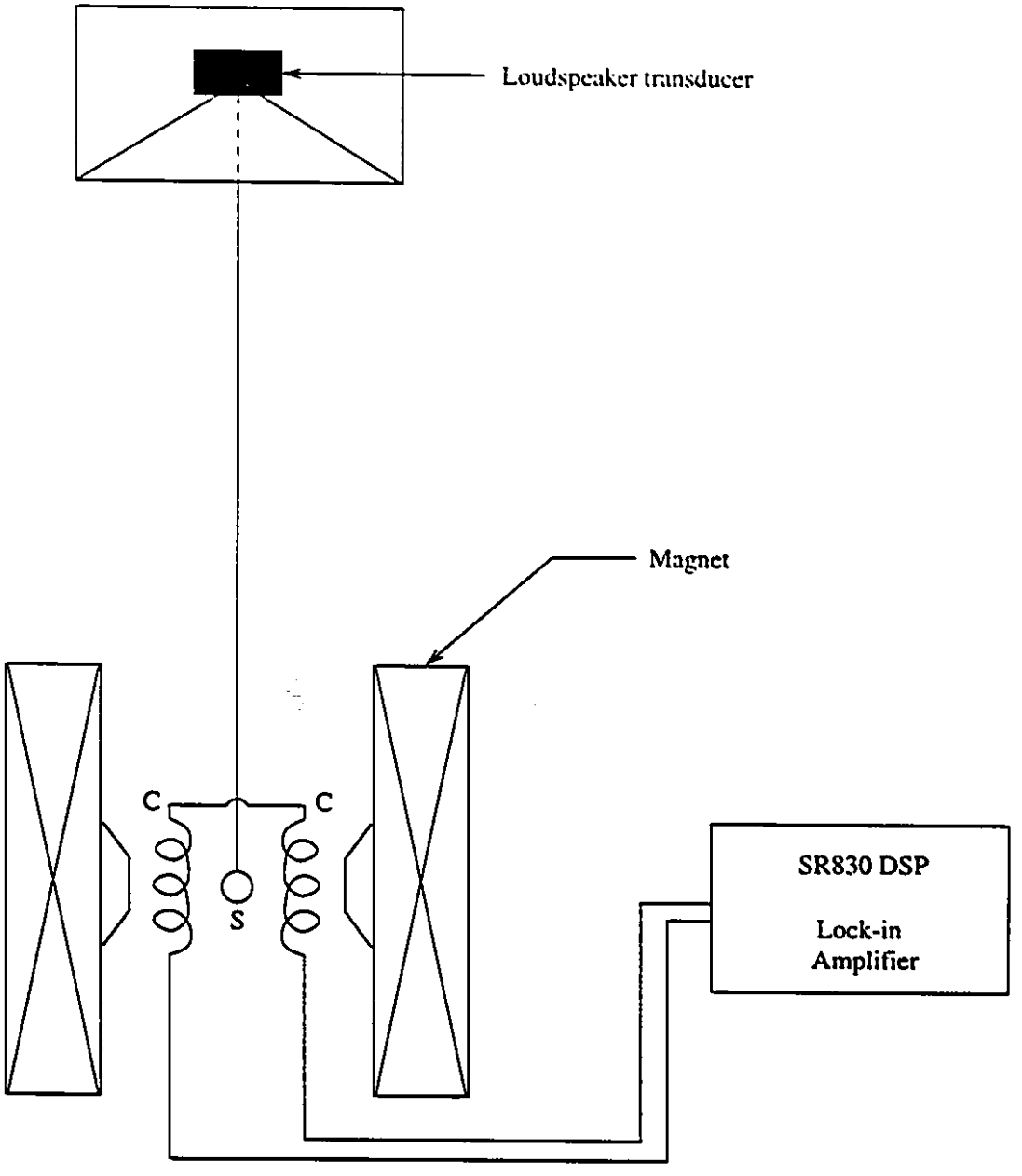

Figure 3.7: Schematic drawing of the vibrating sample magnetometer (VSM), showing the sample (S), and the pick-up coils (C).

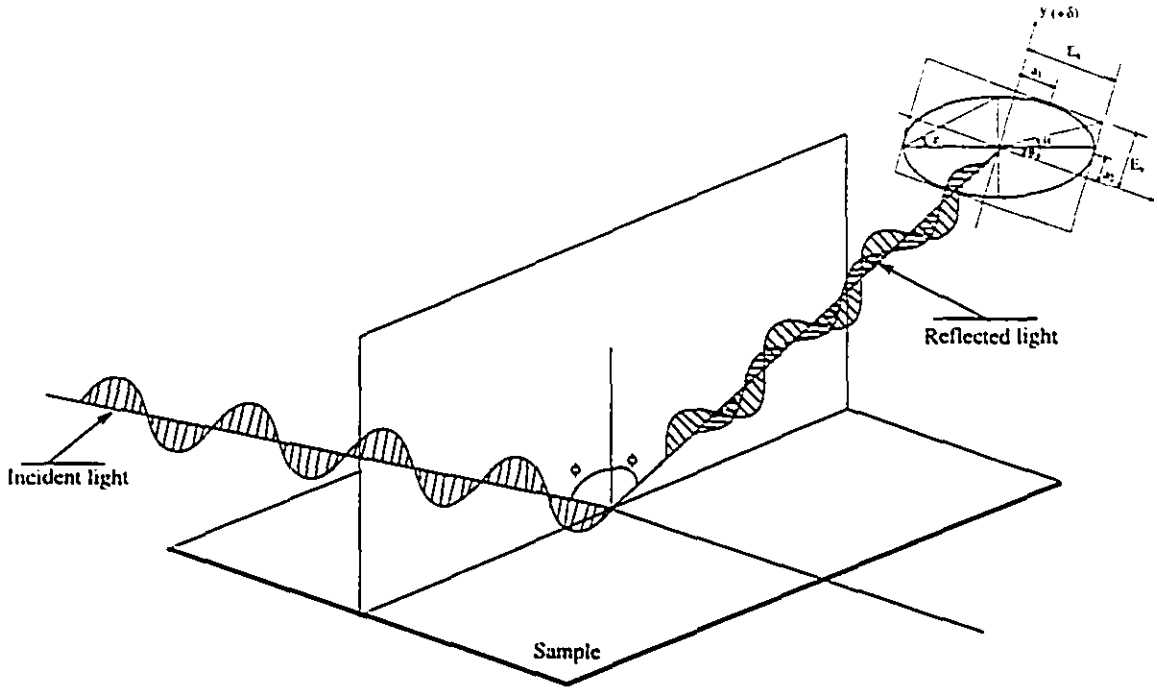

Figure 3.8: Schematic representation of the induced Kerr rotation (θ) and ellipticity (ϵ) at the surface of a magnetized sample.

response that is in phase with the incident light gives rise to the rotation, while the component out of phase accounts for the ellipticity. When an external magnetic field is applied to reverse the magnetization of the sample, the Kerr rotation and ellipticity also reverse sign. The appeal of this particular technique arises from the result that, to first-order approximation, the Kerr rotation and ellipticity are proportional to the magnetization of the film. Details of this derivation can be found in the references[40, 41]. A simple measurement of Kerr rotation, θ, versus applied field, H, corresponds therefore to the M versus H hysteresis loop.

Figure 3.9 shows schematically the apparatus used to detect MOKE signals. In this set-up, the light source is a He-Ne laser which is linearly polarized. The reflected light that has been elliptically polarized by the medium passes through another polarizer (which acts as the analyzer), whose polarization axis is nearly crossed with the incident beam. It is then detected by a photodiode which is covered by a filter that only transmits He-Ne light. As the applied magnetic field is swept to reverse the magnetization of the sample, the intensity of light reaching the detector changes.

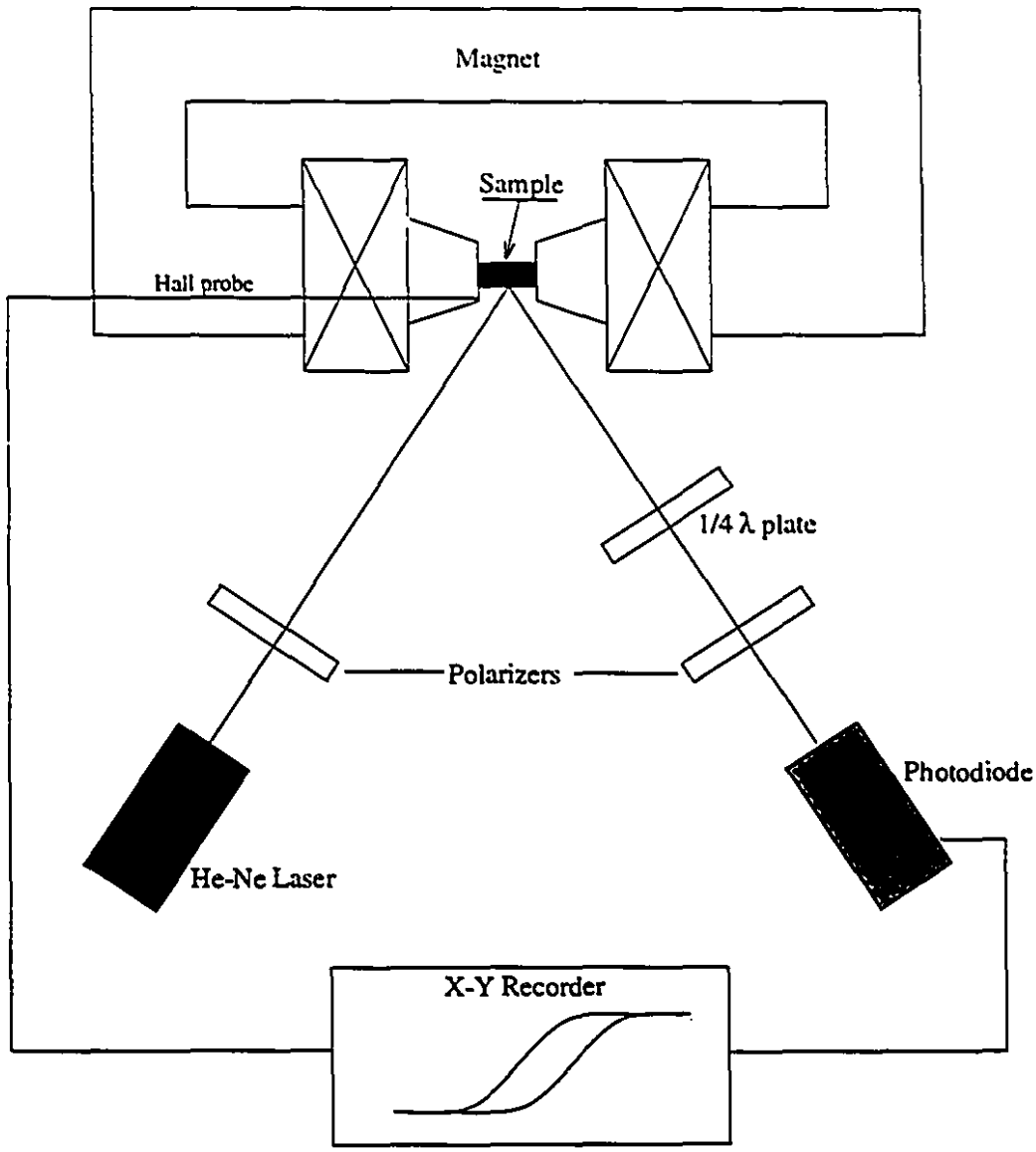

Figure 3.9: Schematic configuration of longitudinal magneto-optic Kerr effect magnetometer.

Thus the output of the detector versus applied field yields the magnetic hysteresis loop of the sample. All measurements were performed ex-situ at room temperatures in fields up to 0.8 Tesla applied in the plane of the film and the scattering plane of the light.

3.4 Magnetotransport Measurements

The most important transport measurement in this research is magnetoresistance (MR). The term magnetoresistance refers to the variation of resistance, ρ, of the sample as a function of applied magnetic field, H. It is commonly defined with respect to the resistance at saturation magnetic field, H_s, as:

$$\frac{\Delta\rho}{\rho} = \frac{\rho(H) - \rho(H_s)}{\rho(H_s)} \tag{3.3}$$

All transport properties were measured using a four probe high-resolution ac bridge designed by Cochrane, Kästner and Muir[42] in applied fields up to 1.0 Tesla. The magnet can be rotated to obtain a field parallel or perpendicular to the film plane. The block and circuit diagrams for this apparatus are shown in Fig. 3.10. The basic measurement method consists of driving separate but identical alternating currents through the sample (S) and a standard resistance (R_s). The standard voltage is divided by an inductive voltage driver and compared with the signal across the sample using a lock-in amplifier. In this configuration, the apparatus is a direct reading linear deviation resistance bridge employing the four-terminal geometry necessary for detecting small resistance values. Since the lock-in amplifier is used in a null-detection mode and fluctuations in the oscillator current are cancelled to first order[43], the apparatus is very sensitive to small resistance changes. The essential feature of this technique is that the transformers T_1 and T_2 are linked together in such a way that a change in the current of one loop (due, for instance, to a change in sample resistance) induces a corresponding change in the other loop. The sensitivity of this apparatus is $\sim 5\times10^{-6}$ Ω and allows measurement of resistances between 10^{-2} and 10^{2} Ω. All magnetotransport experiments in this research were performed at room temperature.

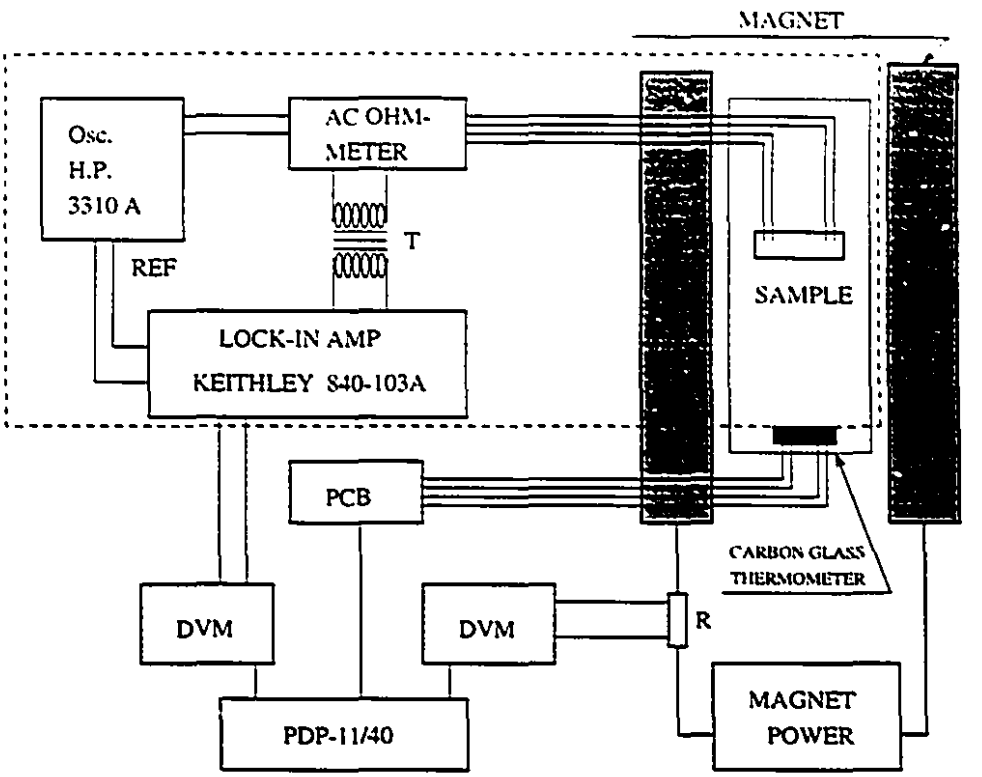

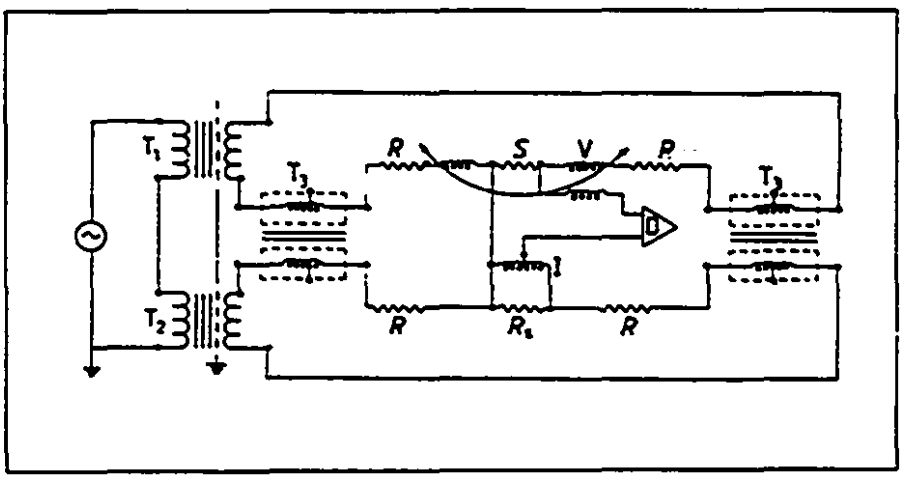

Figure 3.10: Block and circuit diagrams for the high-resolution ac bridge.

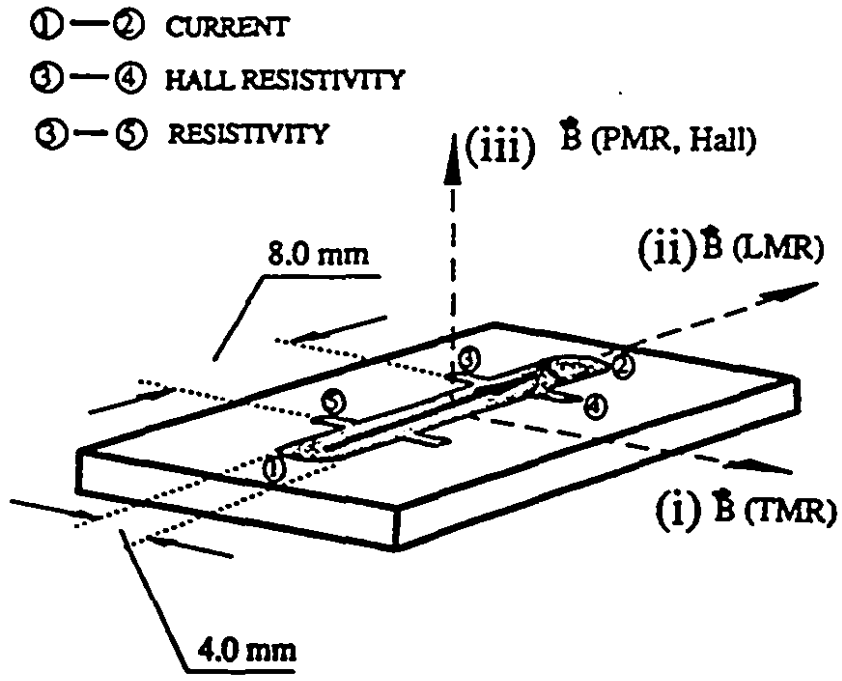

Figure 3.11: Sample dimensions and geometry for the magnetotransport measurements.

The sample configuration as defined by a contact mask during deposition and suitable for electrical transport measurements is shown in Fig. 3.11. The mask defines a sample surface 4.0 mm wide with two small arms for electrical contacts 8.0 mm apart. Current is applied across contacts 1 and 2 using conductive silver paste to ensure electrical contact between sample and leads. Magnetoresistance is measured across contacts 3 and 5, with the applied field in three orientations: (i) field in plane and perpendicular to current, transverse MR (TMR); (ii) field in plane and parallel to current, longitudinal MR (LMR); (iii) field perpendicular to film plane, perpendicular MR (PMR). Finally, Hall resistivity was measured across contacts 3 and 4 in the same field orientations described above.

4

Results and Discussion

IN THIS CHAPTER we present and analyze the experimental results of our study of Ni/Co multilayers. The first section gives the structural characterization of the multilayers performed by grazing-angle X-ray reflectivity and high-angle X-ray diffraction experiments. Results from the magnetic measurements by VSM and MOKE, examining magnetization and magnetic anisotropy, are then presented. Finally, the magnetotransport measurements are shown and correlated to the structural and magnetic properties of these multilayers.

4.1 Structural Characterization

4.1.1 Grazing-Angle X-ray Reflectivity Analysis

Grazing-angle X-ray reflectivity experiments are paramount in the characterization of the structure of multilayered thin films. By modelling the multilayers and comparing the calculated X-ray spectra of the modelled structures to the experimental data, one can obtain detailed quantitative structural information such as the bilayer period Λ and the interfacial mixing[44, 45], i.e., the region of atomic interdiffusion at the interface between two layers.

Optical Model for Reflectivity Calculations

The X-ray reflectivity is based on a standard optical model[46]. Consider an incoming X-ray beam illuminating the surface of a crystal. The index of refraction in the X-ray wavelength range is slightly less than 1, and can be expressed as $n = 1-\delta-i\beta$, where

δ and β can be written as

$$\delta = \frac{\mathcal{N}_o r_e \lambda^2}{2\pi}(f_o + \Delta f') = \frac{r_e \lambda^2}{2\pi}\rho_e \tag{4.1}$$

$$\beta = \frac{\mathcal{N}_o r_e \lambda^2}{2\pi}\Delta f'' = \frac{\lambda}{4\pi}\mu \tag{4.2}$$

where r_e is the classical electron radius $e^2/mc^2 = 2.818 \times 10^{-13}$ cm, $\mathcal{N}_o$ is the number density of atoms, λ is the X-ray wavelength, f_o is the atomic scattering factor at zero momentum transfer (equal to $\mathcal{Z}$, the atomic number of the atom under consideration), $\Delta f'$ and $\Delta f''$ are the real and imaginary parts of the dispersion corrections to f_o, ρ_e is the electron density and μ is the linear absorption coefficient. The critical angle for total external reflection $\theta_c \approx \sqrt{2\delta}$ has values typically in the range $0.2° - 0.6°$ using X-rays of wavelength around 1.5 Å[47]. At incidence angles greater than this critical angle, most of the X-ray beam is refracted into the material, allowing interference between reflections from various interfaces, including the upper surface. The highly periodic structure along the film growth direction in a multilayer sample leads to constructive interference and superlattice Bragg peaks with positions determined by the modified Bragg law[48]

$$\sin^2\theta = \sin^2\theta_B + 2\delta \tag{4.3}$$

or simply (since for small x, $\sin x \approx x$)

$$\theta^2 = \theta_B^2 + \theta_c^2 \tag{4.4}$$

where θ is the measured position of the diffraction peak, and θ_B is the position determined from the simple Bragg law (neglecting refraction) $\sin\theta_B = n\lambda/2\Lambda$, where Λ is the modulation wavelength (bilayer period).

The X-ray reflectivity is calculated using a matrix method[46]. Every single layer in the multilayer is characterized by a (2×2) matrix which is a function of the layer thickness t, the complex refractive index n (in terms of the electron density ρ_e and the linear absorption coefficient μ, Cf. eqs. 4.1-4.2) and the wave vector ($\kappa_o = 2\pi/\lambda$) of the incident beam. The total multilayer matrix is obtained from a product of these individual layer matrices. Possible interfacial mixing is assumed to have a linear

composition profile and is treated as a sequence of slices ($\sim$ 1 Å) with an average index of refraction for which the appropriate matrix is calculated. For example, the average electron density ρ_e^m of the mth slice of an interface is given by

$$\rho_e^m = \rho_e^A + m\frac{\rho_e^B - \rho_e^A}{M+1} \tag{4.5}$$

where ρ_e^A and ρ_e^B are the electron densities of the pure materials A and B, respectively, and M is the number of slices. The average linear absorption coefficient is similarly defined. The global interface roughness is incorporated into the model calculation by assuming a Gaussian form (with a Debye-Waller factor to include the effect of thermal vibrations of the ions about their equilibrium positions) to simulate the damping effect[49]. Thus the specular reflection intensity R from a rough multilayer is given by

$$R = |r|^2 e^{-\sigma_r^2 q^2} \tag{4.6}$$

where r is the reflection coefficient of a multilayer with smooth interfaces, $q = 4\pi \sin\theta/\lambda$ is the scattering vector, and σ_r is the root mean square (rms) value of roughness.

A computer program developed originally by M. Sutton's group of McGill University and Y. Huai, R Cochrane of Université de Montréal[49, 50] was employed to calculate the grazing angle reflectivities from the above optical model. The model calculations are fitted to the data using a non-linear least squares procedure that minimizes χ^2 defined as

$$\chi^2 = \sum_{i=1}^{M}(R_i^m - R_i^c)^2/\sigma_i^2 \tag{4.7}$$

where R_i^m and R_i^c are the experimental and calculated X-ray reflected intensities, respectively, M is the total number of data points and σ_i^2 is the weighting function.

Whereas this fitting procedure is widely used and, in general, successful in quantitative X-ray analysis, the large number of parameters that are required leads, in certain situations, to a degeneracy in some of these parameters.

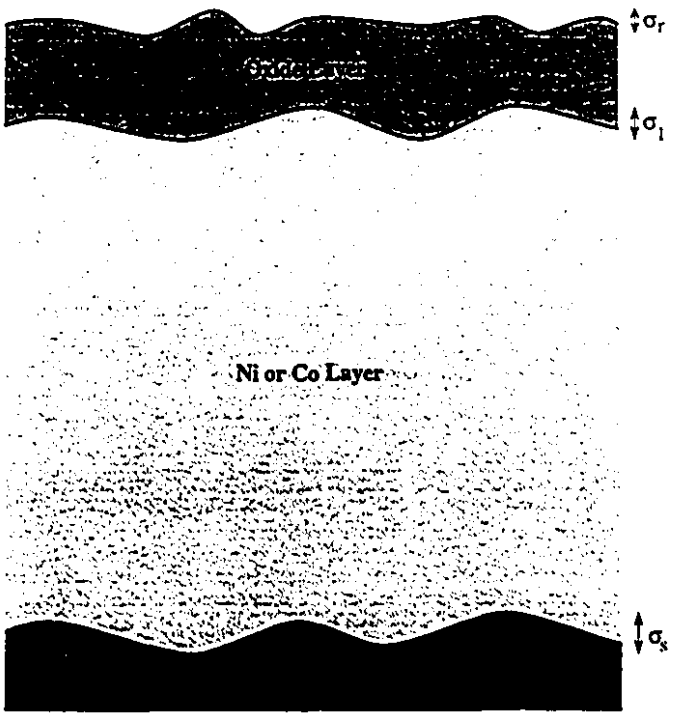

Figure 4.1: Schematic representation of the fitting parameters used in the X-ray fitting procedure on single layer thin film samples.

Single Layer Results

For the purpose of calibrating the deposition rates in the magnetron sputtering system (Cf. Sec. 3.1), two single films of Ni and Co were prepared. Since the thicknesses of these films are comparable to the total thickness of the multilayer samples, it is possible to compare the total surface roughnesses of the simple and multilayered structures. In the model calculations, an oxide layer on top of the sample was assumed to account for the exposure to air. Optimization of the fit is achieved by varying the thicknesses of the film and oxide layers, the roughnesses of the substrate and Ni or Co layer, and the rms outer surface roughness σ_r. Figure 4.1 illustrates these fitting parameters.

Figure 4.2 presents the X-ray reflectivity data (dots) and the calculated spectra (solid line) for the two single layer films deposited on oxidized silicon substrates. The

Table 4.1: Structural parameters extracted from the fitted results shown in Fig. 4.2 for the single layer Ni and Co samples. The captions are: σ_s, substrate roughness; t_l, Ni or Co layer thickness; σ_l, Ni or Co layer roughness; t_o, oxide layer thickness; σ_r, outer surface roughness.

Sample	σ_s (Å)	t_l (Å)	σ_l (Å)	t_o (Å)	σ_r (Å)
SiO_2/Ni1000Å	7.5 ± 0.2	1027.1 ± 0.3	4.2 ± 0.1	9.9 ± 1.7	9.0 ± 2.4
SiO_2/Co500Å	11.7	509.7	8.9	38.1	8.8

data and calculated results are plotted on a semilog scale as a function of the scattering vector $q = 4\pi \sin\theta/\lambda$. The electron densities and the linear absorption coefficients of bulk Ni and Co were used in the calculations. As can be seen in Fig. 4.2, excellent agreement between the fitted and experimental data is achieved. The actual layer thicknesses were found to be within $\sim \pm 10\%$ of the nominal values. In both samples, an oxide overlayer with approximately 30% of the electron density of Ni or Co was added, with the Co single-layer necessitating a much thicker oxide layer. Similar thickness oxidation layers have been reported in X-ray diffraction studies of Co/Re superlattices when Co is the top layer[51]. The layer roughness σ_l deduced for the Co single-layer sample was larger than that deduced in the Ni sample. Furthermore, it was necessary in both samples to introduce an outer surface roughness to obtain good fits. The fitted parameters for both single layer samples are summarized in Table 4.1.

In general, grazing-angle reflectivity measurements are sensitive to the average electron density ρ_e along the film growth direction irrespective of the crystalline quality of the sample. As previously mentioned, the refractive index of a crystal surface for X-rays is slightly less than unity. Consequently, below a certain critical angle θ_c, total reflection occurs at the surface, and the average electron density at the film surface can be obtained from $\theta_c \propto \sqrt{\rho_e}$. The critical angles for Ni and Co, as read off the spectra, are $2\theta_c \approx 0.76°$ ($q_c = 0.054$ Å^{-1}) and $0.70°$ ($q_c = 0.050$ Å^{-1}), respectively. Beyond θ_c the penetration depth into the film increases and each interface scatters the incoming wave. The superposition of these scattered amplitudes leads to an interference effect. Thus, the two interfaces of the single layer films give rise to

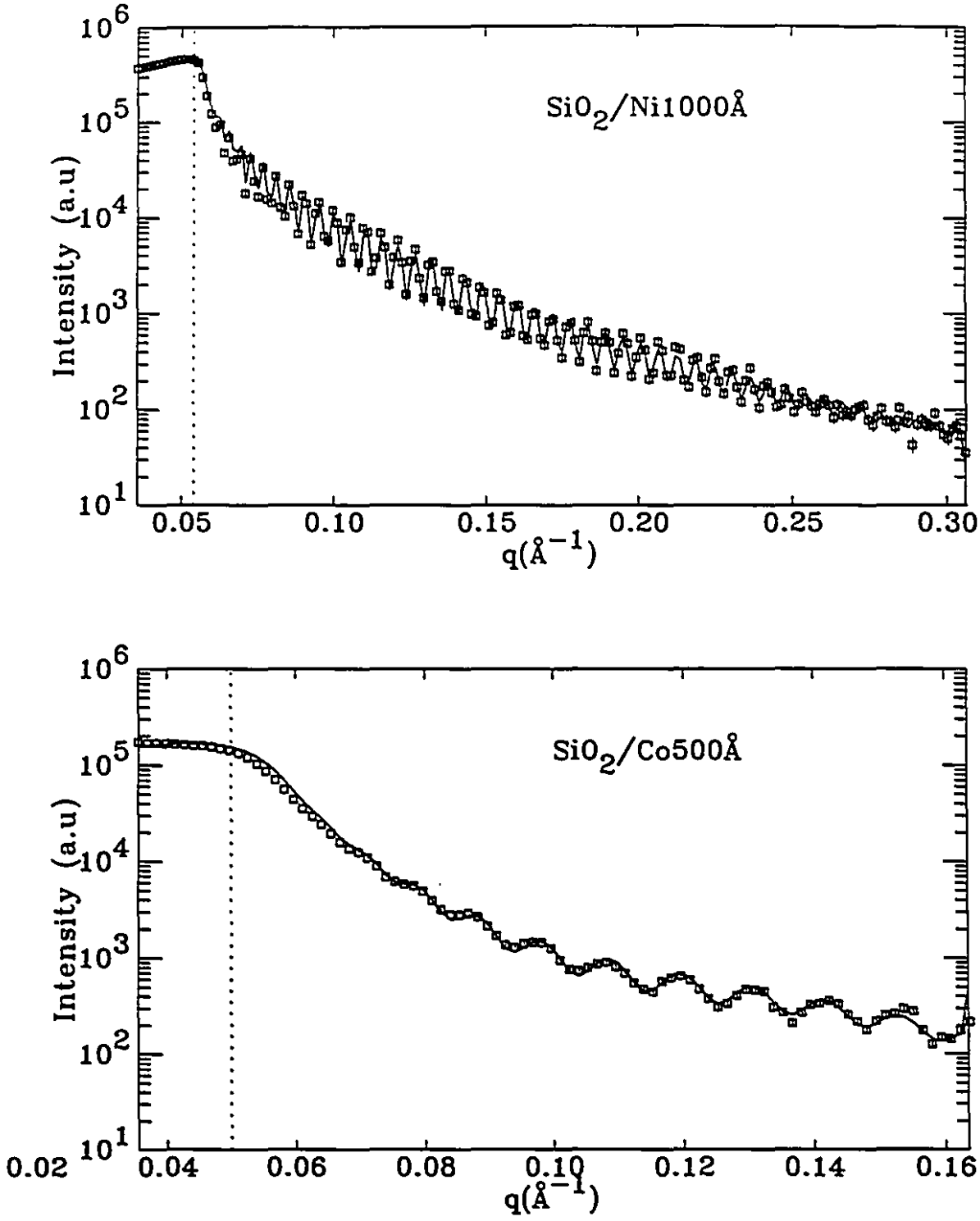

Figure 4.2: Grazing-angle X-ray reflectivity data and calculated spectra for the two single layer samples listed in Table 4.1. The dots are the data points and the solid line is the calculated result from the optical model. The dotted line shows the approximate position of the critical angle θ_c.

intensity oscillations superimposed on the classical Fresnel reflectivity.

Ni/Co Multilayers

Ni/Co multilayers with bilayer period Λ of 50 Å to 80 Å and bilayer number ranging from 6 to 48 were prepared by DC-sputtering under the conditions listed in Table 3.1 in the previous chapter. Figure 4.3 presents the X-ray reflectivity spectra for the series of multilayers with a fixed Ni layer thickness of 40 Å. Figure 4.4 shows the same for the series with the Co thickness fixed at 40 Å. As can be seen in both figures, along with the total thickness oscillations previously seen in the single layer data, there are additional larger satellite peaks due to the superlattice structure. Since the contrast in the electron densities of Ni and Co is very small, these satellites are expected to be rather weak. Nevertheless, superlattice Bragg peaks up to the fourth-order in both Figs. 4.3 and 4.4 are clearly visible, indicating a well-defined compositional modulation along the film growth direction.

The multilayer reflectivity data were analyzed using the same optical model described in the previous section. The calculated intensity was fitted by adjusting the initial parameters, including the Ni and Co layer thicknesses and roughnesses, and the X-ray detector background, to match the Bragg peak positions and intensities, and the overall profile of the spectrum. The number of superlattice periods is set equal to the actual number of bilayers in the sample. An oxide overlayer of about 20 Å, with an electron density representing roughly 30-40% of the electron density of Co, and an outer surface roughness were added to fine-tune the calculated results. Finally, all the parameters were refined using the non-linear least squares fitting procedure which minimizes χ^2.

Figure 4.5 illustrates a representative fit of the calculated reflectivity to the experimental data in a (Ni30Å/Co40Å)×12 multilayer. The structural parameters extracted from the fitting procedure are in good agreement within 10% of the nominal values and are listed in Table 4.2. The roughnesses of the individual Ni and Co layers were found to vary between 5.0 Å and 7.9 Å in all samples with 12 bilayers, independent of composition; measured roughness sets an upper-bound on the size of the interdiffused

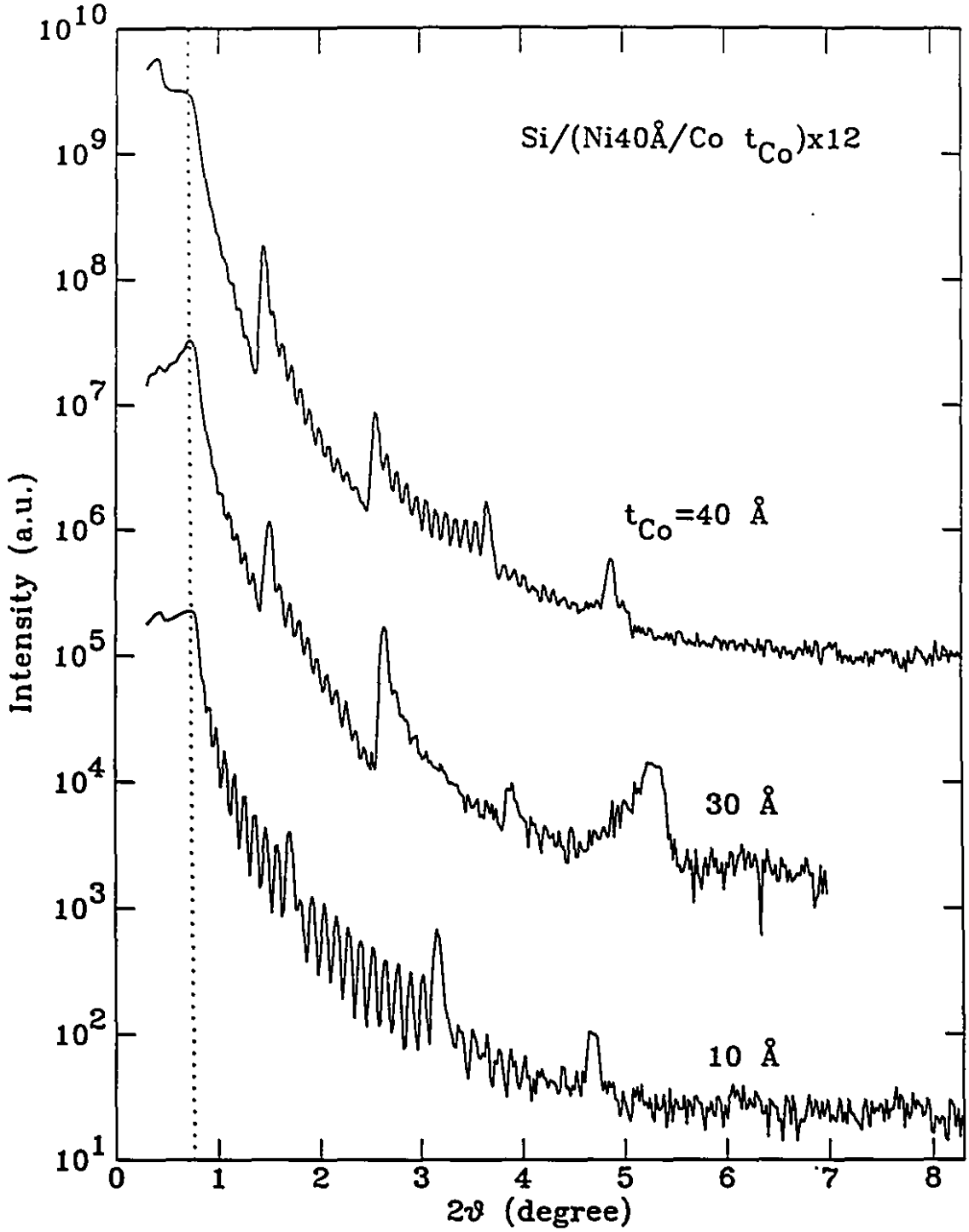

Figure 4.3: Grazing-angle X-ray reflectivity data for a series of (Ni40Å/Cot_{Co})×12 multilayers with constant t_{Ni} = 40 Å and t_{Co} = 40, 30, and 10 Å. For clarity, the spectra have been shifted vertically.

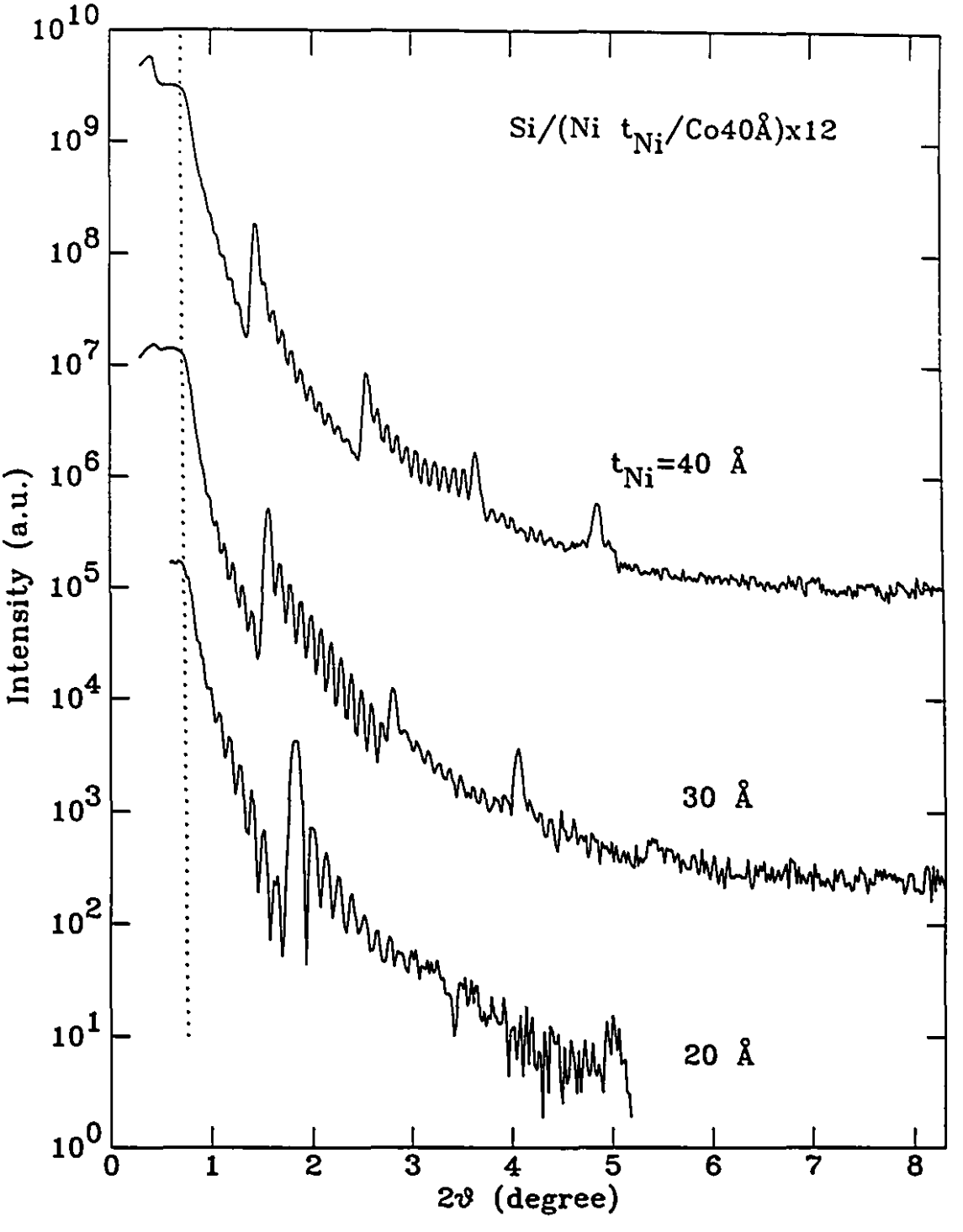

Figure 4.4: Grazing-angle X-ray reflectivity data for a series of (Nit$_{Ni}$/Co40Å)×12 multilayers with constant t_{Co} = 40 Å and t_{Ni} = 40, 30, and 20 Å. For clarity, the spectra have been shifted vertically.

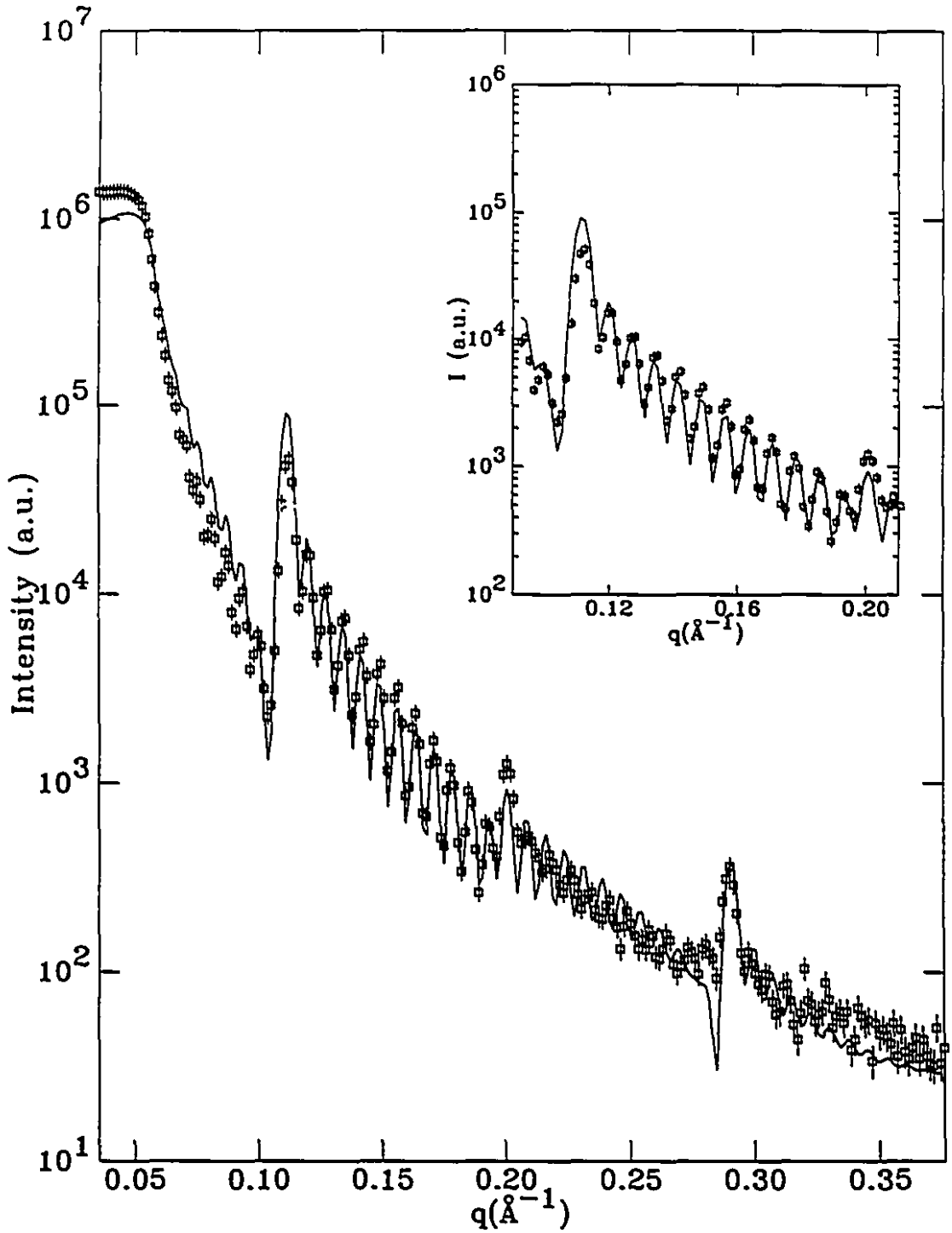

Figure 4.5: Grazing-angle X-ray reflectivity data and calculated spectrum for a (Ni30Å/Co40Å)×12 multilayer. Inset is a close-up of the first two superlattice Bragg peaks. The dots are the data points and the solid line is the calculated result from the optical model with the parameters listed in Table 4.2.

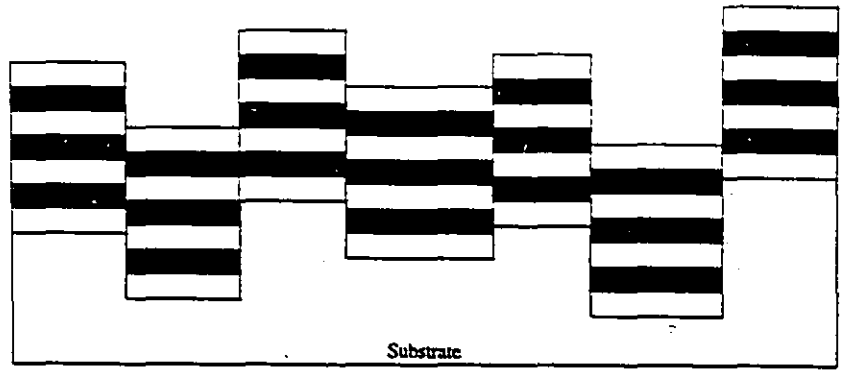

Figure 4.6: Possible island structure leading to high layer and surface roughnesses while retaining higher-order superlattice peaks.

region in these multilayers. The relatively thick oxide layer of $\sim$ 20 Å required to obtain good fits reflects the fact that the top layer of each multilayer was Co, which was shown, in the previous section, to give thicker oxide layers. The outer surface roughness σ_r extracted from the fits and varying from 2.0 Å to 5.5 Å in the multilayers with $N = 12$, was significantly larger for samples with thin layers of Ni or Co and is likely to be responsible for the smearing-out of the fourth-order superlattice peak in the $t_{Co} = 10$ Å sample. The structural imperfections in this sample may be ascribed to strong interdiffusion and alloying at the interfaces [52]. The same behaviour is seen in the $t_{Co} = 5$ Å samples with σ_r exceeding 5.9 Å. Remarkably, the value of the roughness of the Co layer in the Si/(Ni40Å/Co5Å)×48 multilayer, deduced by structural refinement, exceeds the thickness of this layer, suggesting the diffusion and alloying of the entire Co layer into the surrounding Ni layers. Alternatively, in these samples, an island structure of dislocated sub-multilayers may have formed as shown in Fig. 4.6. This would offer an explanation to the high values of roughness obtained in the fits despite the observation of higher-order superlattice peaks, since, individually, the small multilayer islands would produce the constructive interference at the superlattice Bragg peaks.

Structural Dependence on Bilayer Repetition Number

Figure 4.7 shows a series of (Ni40Å/Co5Å)×N multilayers with the number of bilayers N varying from 6 to 48. The relevant parameters extracted from the X-ray

Table 4.2: Structural parameters extracted from fitting the X-ray reflectivity data for Ni/Co multilayers deposited on Si. Here, Λ is the bilayer period, t_o is the oxide layer thickness, t_{Ni} and t_{Co} are the Ni and Co layer thicknesses, respectively, σ_{Ni} and σ_{Co} are the Ni and Co layer roughnesses, respectively, σ_s is the substrate roughness, and σ_r is the outer surface roughness.

(Ni/Co)×N	Λ (Å)	t_o (Å)	t_{Ni} (Å)	t_{Co} (Å)	σ_{Ni} (Å)	σ_{Co} (Å)	σ_s (Å)	σ_r (Å)
(40Å/40Å)×12	73.8	21.6	42.1	31.8	7.0	7.0	12.0	2.8
(40Å/30Å)×12	70.9	24.0	48.7	22.2	5.5	5.5	10.0	3.6
(40Å/20Å)×12	63.5	27.1	48.0	15.5	6.0	7.9	6.3	4.7
(40Å/10Å)×12	58.5	23.0	47.0	11.5	5.0	5.0	7.0	5.5
(30Å/40Å)×12	67.0	22.0	37.0	30.0	6.0	5.0	8.5	2.0
(20Å/40Å)×12	54.1	17.2	32.6	21.6	7.0	5.4	8.1	5.5
(40Å/5Å)×6	53.9	27.7	49.2	4.7	4.2	4.7	6.0	5.9
(40Å/5Å)×24	53.0	17.1	48.0	5.0	5.2	4.9	8.0	6.6
(40Å/5Å)×48	52.9	18.7	50.3	2.6	5.2	4.1	6.2	9.5

fitting procedure are also shown in Table 4.2. Most significantly, the outer surface roughness increases considerably as N is increased. Qualitatively, this is evidenced by the reduction in intensity of the total thickness oscillations (or lattice fringes) between the superlattice Bragg peaks. In fact, for finite film thickness ($\sim$ 1000 Å), the suppression of lattice fringes with increasing N is partially correlated to an increased outer surface roughness[49]. The values of the layer roughnesses σ_{Ni} and σ_{Co} were also found to increase slightly with N. This observation is consistent with an accumulation of small thickness fluctuations associated with each layer[53, 54]

4.1.2 *High-Angle X-ray Diffraction Analysis*

High-angle X-ray diffraction measurements with the scattering vector perpendicular to the film surface provide information on the atomic order along the growth direction. Figure 4.8 illustrates the high-angle X-ray diffraction spectrum for a (Ni40Å/Co40Å)×12 multilayer deposited on a Si (100) wafer. The main diffraction

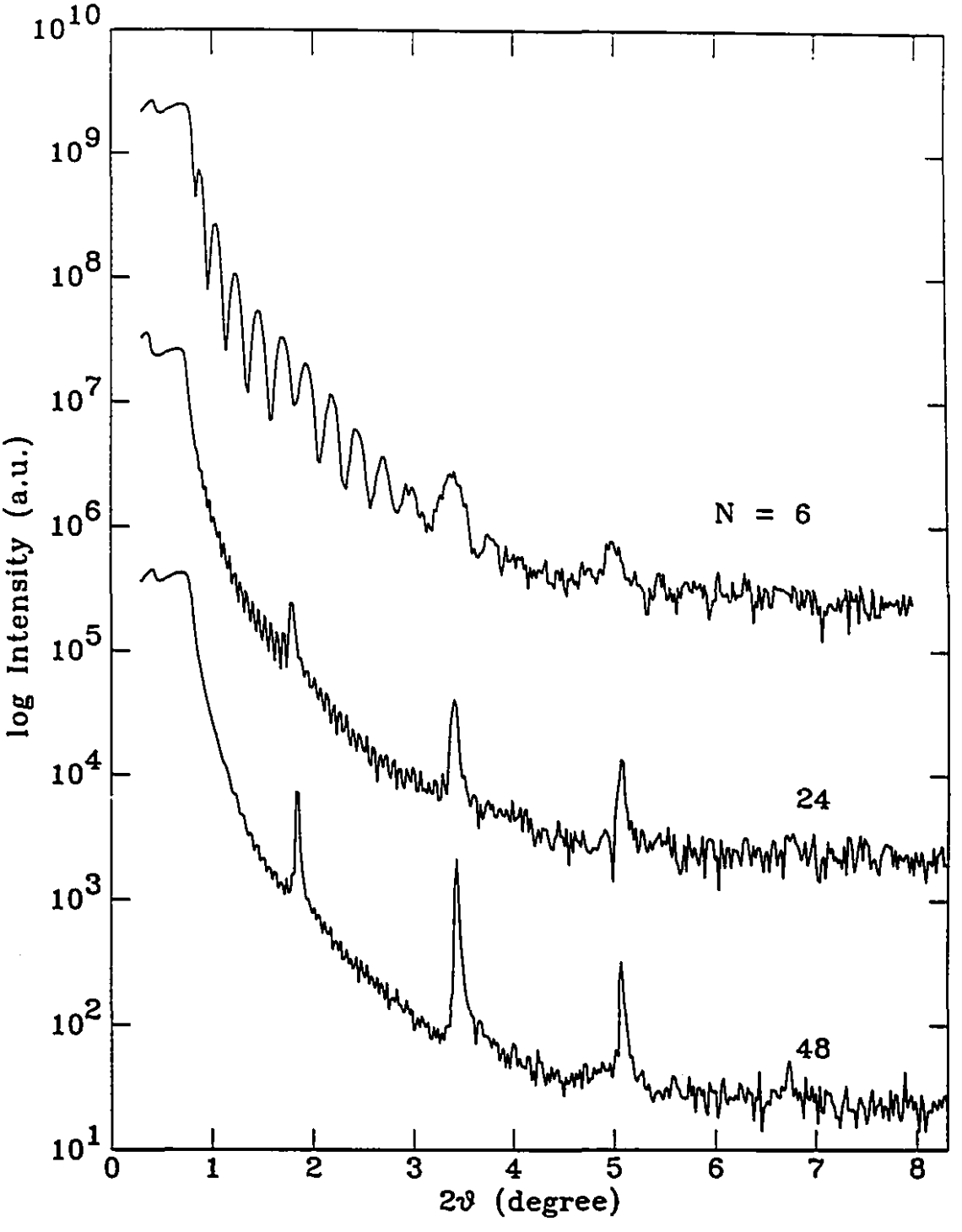

Figure 4.7: Grazing-angle X-ray reflectivity data for a series of (Ni40Å/Co5Å)×N multilayers with number of bilayer repetitions N varying from 6 to 48. For clarity, the spectra have been shifted vertically.

peak at $2\theta \sim 44.6°$ corresponds to a weighted average of Ni(111) and Co(111) Bragg peaks. Similarly, the peak at $2\theta \sim 51.7°$ corresponds to the (200) peaks of Ni and Co. The other peaks shown are satellite peaks due to the superlattice periodicity. Co grows in its FCC phase as demonstrated by the fact that the main Bragg peak moves from a position corresponding to $d_{Ni}(111) = 2.034$ Å to a position corresponding to $d_{Co}^{FCC}(111) = 2.046$ Å as the total proportion of Co is increased. If Co grew in its HCP phase, then the diffraction peak would move to the $d_{Co}^{HCP}(0002) = 2.023$ Å position. The second peak corresponding to a weighted average of Ni(200) and Co(200) also behaves in the same manner, shifting from $d_{Ni}(200) = 1.762$ Å to $d_{Co}^{FCC}(200) = 1.772$ Å.

The ratio of the intensities of the (111) and (200) peaks, $I_{(111)}/I_{(200)} \geq 10$, indicates that the films have a polycrystalline structure with a preferred (111) orientation and a fraction of (200) structural domains. An ideal polycrystalline structure would have an intensity ratio $I_{(111)}/I_{(200)} \approx 2.0$. The presence of clear superlattice satellite peaks in the diffraction pattern, at positions consistent with the bilayer period Λ obtained by grazing-angle X-ray measurement, suggests a long crystalline coherence length ($\sim$ 450 Å, as estimated from the full-width at half maximum [FWHM] of the (111) Bragg peak in Fig. 4.8) and a well-defined superlattice structure.

4.2 Magnetization Curve Measurements

As was previously stated in Chapter 2, the anisotropic magnetoresistance (AMR) in ferromagnetic transition metals depends on the direction of the sample magnetization with respect to the direction of the applied current. A characterization of the magnetization process is therefore vital to the study of AMR in this system of multilayers.

4.2.1 Vibrating Sample Magnetometry (VSM) Measurements

The magnetization curves for the series of Ni/Co multilayers were measured by VSM with the field applied in the plane of the films. Figure 4.9 shows typical magnetic

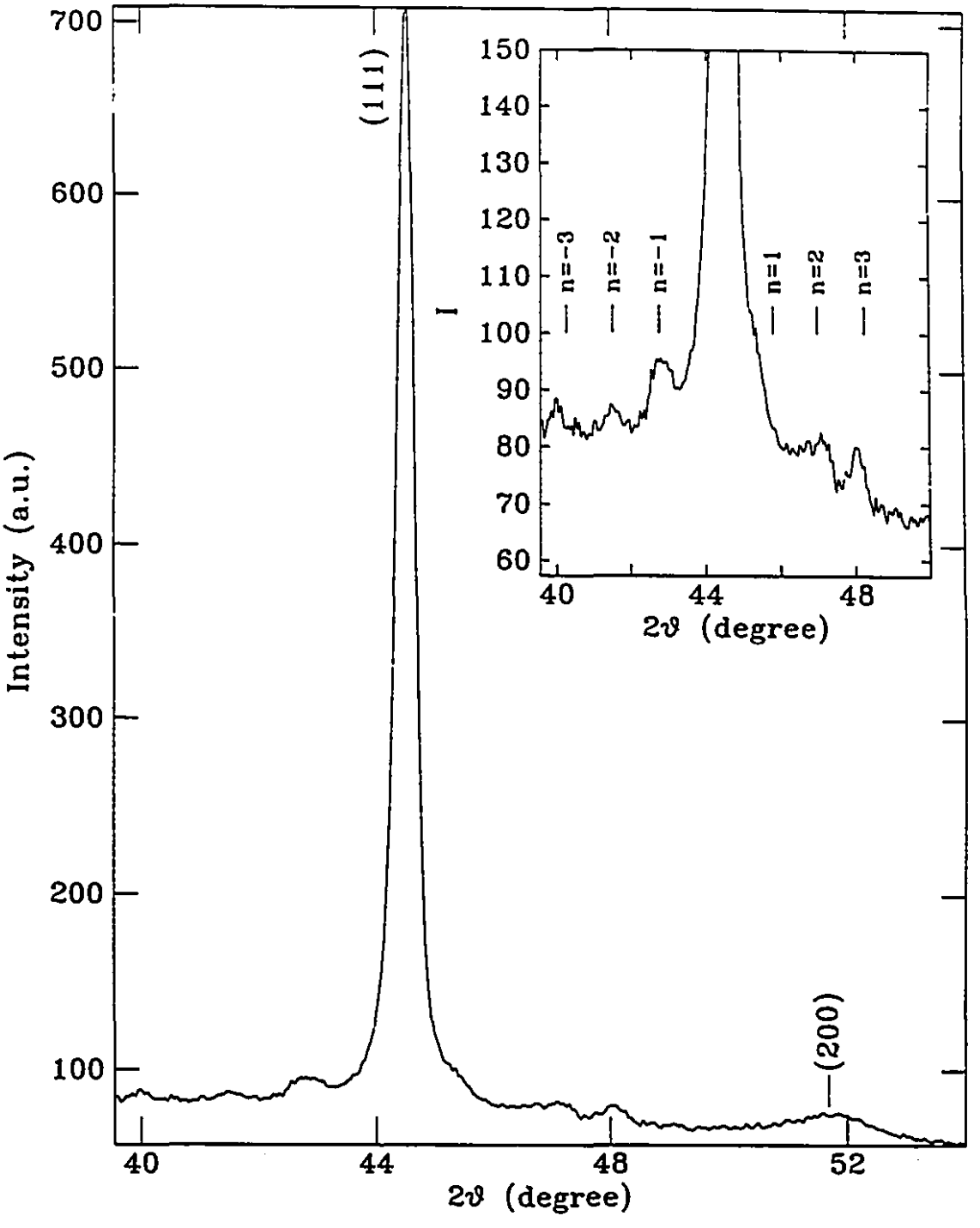

Figure 4.8: High-angle X-ray diffraction pattern for a Si/(Ni40Å/Co30Å)×12 multilayer displaying a polycrystalline structure with a preferred (111) orientation. The inset is an enlarged view showing the superlattice satellite peaks around the main (111) Bragg peak.

hysteresis loops for a Ni/Co multilayer with the field applied in the longitudinal and transverse directions, i.e., along the long and short axes of the rectangular film, respectively. As can be seen in the figure, these multilayers exhibit a strong in-plane magnetic anisotropy, with an easy axis of magnetization in a direction making an angle between 90° and 105° with respect to the longitudinal axis. The remanent magnetization (M_r/M_s) is as low as 0.25 in some samples with field applied along a hard-axis. The variation of the remanence as a function of the in-plane angle θ of the applied field is shown in Fig. 4.10, with the presence of the easy-axis indicated by the position of the maximum around $\theta = 105°$. The existence of this in-plane easy-axis is consistent with previous results on Ni/Co[13] and Ni/Fe[55] multilayers. In the present Ni/Co system, in which the growth of FCC Co has been established, it is not unreasonable to expect the magnetization to lie in plane. Although perpendicular magnetic anisotropy (PMA) has been reported in ultrathin Ni/Co multilayers[56] with individual layer thicknesses of only 2-3 monolayers (ML), in this study most of the layers are much thicker (≥ 10 Å ≈ 5 ML) and the magnetization therefore favours the in-plane orientation. Moreover, the surface anisotropy term that dominates the shape anisotropy, or demagnetization factor, in PMA thin films is proportional to the flatness of the film. The relatively rough surfaces obtained by sputter deposition therefore inhibit this perpendicular magnetization configuration. The reason for the preferred direction of the in-plane easy-axis between 90° and 105° with respect to the longitudinal axis is not understood and requires further study. A measured residual stray magnetic field of $\sim$ 3-4 Oe at the substrate level in the magnetron sputtering system may be responsible for the formation, parallel to H, of the easy-axis. Residual stress effects due to lattice mismatch between adjacent Ni and Co layers ($a = 2.034$ Å and 2.046 Å for (111) Ni and Co, respectively, giving a mismatch of $\sim 0.6\%$), or the lattice mismatch between the substrate ($a = 2.35$ Å for (111) Si) and first Ni layer (a mismatch of $\sim 13.5\%$) are possible explanations as well, since Ni exhibits a strong negative magnetostriction ($\lambda = -3.4 \times 10^{-5}$)[19].

Table 4.3 shows the magnetization data measured by VSM for the studied multilay-

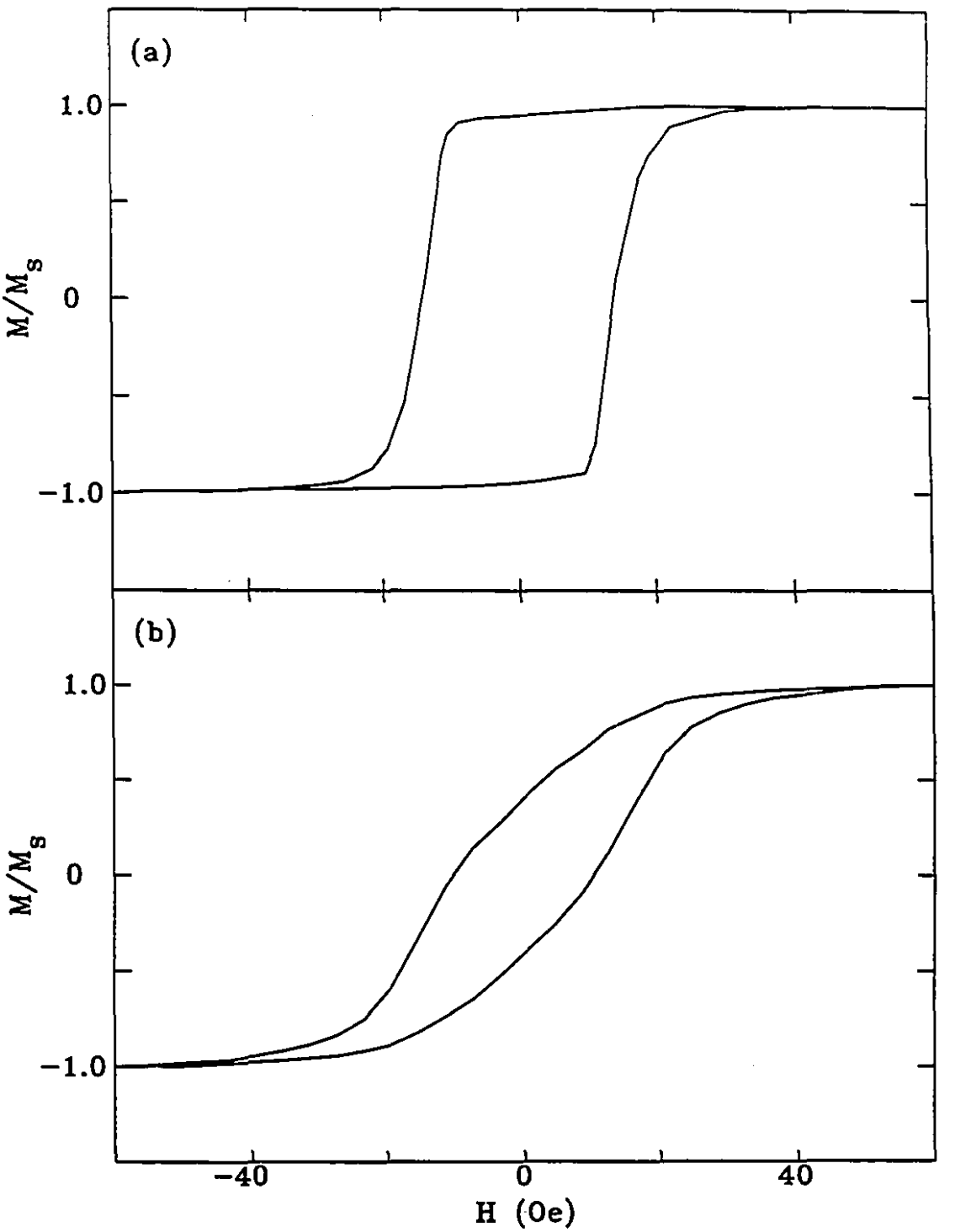

Figure 4.9: Magnetic hysteresis curves measured by VSM on a Si/(Ni40Å/Co10Å)×12 multilayer with field applied in the (a) longitudinal and (b) transverse directions.

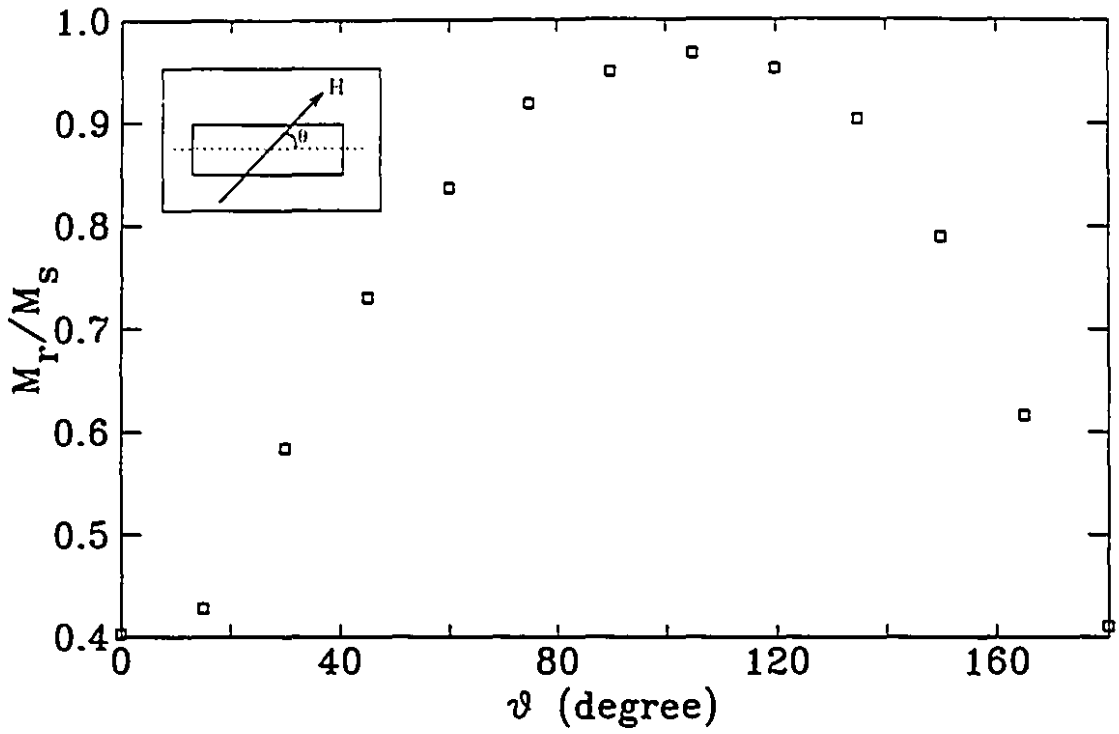

Figure 4.10: Magnetic remanence for a Si/(Ni40Å/Co10Å)×12 multilayer as a function of in-plane angle of applied field θ, as shown in the inset.

ers. The minimum remanent magnetization is given corresponding to the remanence with field applied along a hard-axis (in all samples, with field applied along an easy-axis, the remanence is nearly 1), whereas both minimum and maximum values of coercivity are presented. These values were not found to be correlated to the positions of the easy and hard axes, nor was any correlation with composition found. In fact, coercivity depends strongly on the magnetization process, i.e., domain-wall motion as opposed to coherent rotation of the magnetization, which in turn depends on the structure of the films, as well as the magnetostriction and residual stresses associated with the substrate and magnetic layers. Coercivity is therefore difficult to control and cannot be regarded as a fundamental parameter. Whereas care was taken to ensure uniformity in the deposition conditions, small variations in vacuum quality, substrate quality and temperature, and deposition rates may be responsible

Table 4.3: Magnetic parameters measured by VSM on Ni/Co multilayers. M_s is the saturation magnetization, M_r, the remanence, H_s, the saturation magnetic field, and H_c(max) and H_c(min) are the maximum and minimum coercive fields, respectively.

Sample	$4\pi M_s$ (G)	M_r/M_s(min)	H_s (Oe)	H_c(max) (Oe)	H_c(min) (Oe)
(Ni40Å/Co40Å)×12	11963 ± 600	0.27	53.9	8.7	6.6
(Ni40Å/Co30Å)×12	7389	0.38	42.5	7.4	6.2
(Ni40Å/Co20Å)×12	7653	0.25	47.2	9.5	6.9
(Ni40Å/Co10Å)×12	6409	0.40	61.1	14.2	10.2
(Ni30Å/Co40Å)×12		0.60	38.0	15.8	13.4
(Ni20Å/Co40Å)×12		0.28	56.0	9.5	6.6

for the observed spread in the values of coercivity.

4.2.2 *Magneto-optic Kerr Effect (MOKE) Measurements*

An additional technique used to characterize the magnetzation of the multilayers was magneto-optic Kerr effect (MOKE). MOKE magnetometry provides fast, non-destructive, and in some cases in-situ characterization of the sample. Specifically, since the light penetration is limited (for the case of the $\lambda = 6328$ Å laser used in this study, the penetration on a Co surface is roughly 200 Å), MOKE signals are more sensitive to the surface magnetization. The main drawback of our MOKE technique is the inability to measure the absolute magnetization of the sample; only the shape of the M-H loop can be measured.

Figure 4.11 shows two typical magnetization curves measured by MOKE on a Si/(Ni40Å/Co5Å)×6 multilayer, with field applied in-plane longitudinally, and transversely. Many of the features observed by VSM were consistent with MOKE measurements. In particular the same easy-axis of in-plane magnetization was observed around 90° with respect to the longitudinal axis of the films. However, in the series Si/(Ni40Å/Co5Å)×N of multilayers with varying number of bilayers N, this in-plane

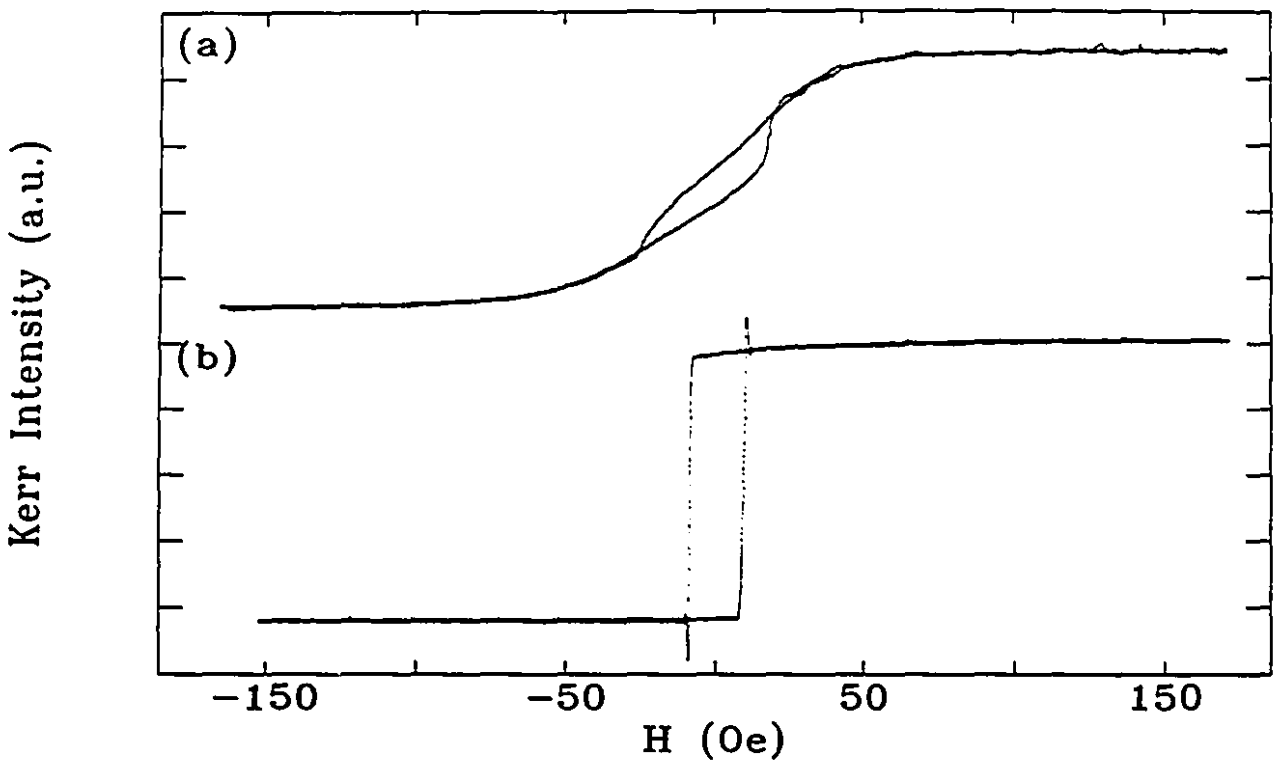

Figure 4.11: MOKE hysteresis loops measured for a Si/(Ni40Å/Co5Å)×6 multilayer with field in-plane (a) longitudinally, and (b) transversely, i.e., rotated through 90°.

easy-axis disappears for the $N = 24$ and 48 samples, suggesting perhaps that the interaction of the substrate with the first layers may be responsible for the formation of the in-plane easy-axis.

4.2.3 *Magnetic Force Microscopy (MFM)*

Magnetic force microscopy (MFM)[57], an offspring of atomic force miscroscopy, allows the imaging of magnetic structures on a 50-100 nm scale. MFM images are acquired by measuring the response of a sharp magnetic tip mounted on a flexible cantilever. The tip interacts with the stray magnetic field emanating from the sample, and this interaction is detected by measuring changes of either the static deflection or the resonant frequency of the cantilever with a sensitive displacement sensor. The image is formed by raster-scanning the sample with respect to the tip and measuring the interaction as a function of position.

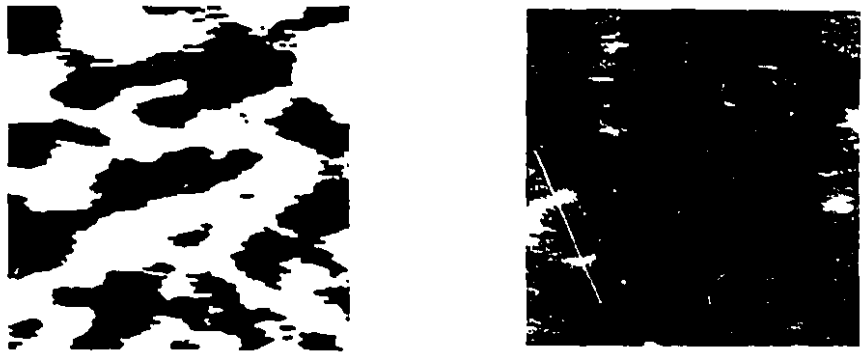

Figure 4.12: MFM images of the magnetic domain structure of the (a) ac-demagnetized and (b) magnetized states in a Si/(Ni40Å/Co5Å)×24 multilayer. The size of the region in (a) is 16 μm × 16 μm; and in (b), 8 μm × 8 μm.

Figure 4.12 illustrates the magnetic domain structure of a Si/(Ni40Å/Co10Å)×24 multilayer measured on the MFM in Peter Grütter's scanning probe microscopy laboratory at McGill University, both in the magnetized and ac-demagnetized states. The contrast in these images, measured using a perpendicularly magnetized cantilever tip, is due to magnetization perpendicular to the plane of the film. In the demagnetized state [Fig. 4.12 (a)], the image displays magnetic domains in an irregular serpentine island structure, with individual islands of $\sim$ 10 μm in length. Preliminary analysis of this domain structure suggests an in-plane magnetic domain structure. Upon magnetization [Fig. 4.12 (b)], the domain structure coalesces into a hexagonal arrangement of domains approximately 2 μm in size. The profile shown in Fig. 4.13 represents the intensity of the measured signal through a section of the domain indicated by the white line in Fig. 4.12 (b). This particular signal profile suggests a perpendicularly magnetized domain structure, which is consistent with the previous observation of the disappearance of the in-plane easy-axis of magnetization.

4.3 *Magnetotransport Properties*

In this section, we describe the results of the magnetotransport measurements performed on the Ni/Co multilayers. We expect these samples to exhibit anisotropic magnetoresistance (AMR), as described in Chapter 2. In a ferromagnetic alloy, this effect has been shown to be strongly correlated to the intrinsic physical properties

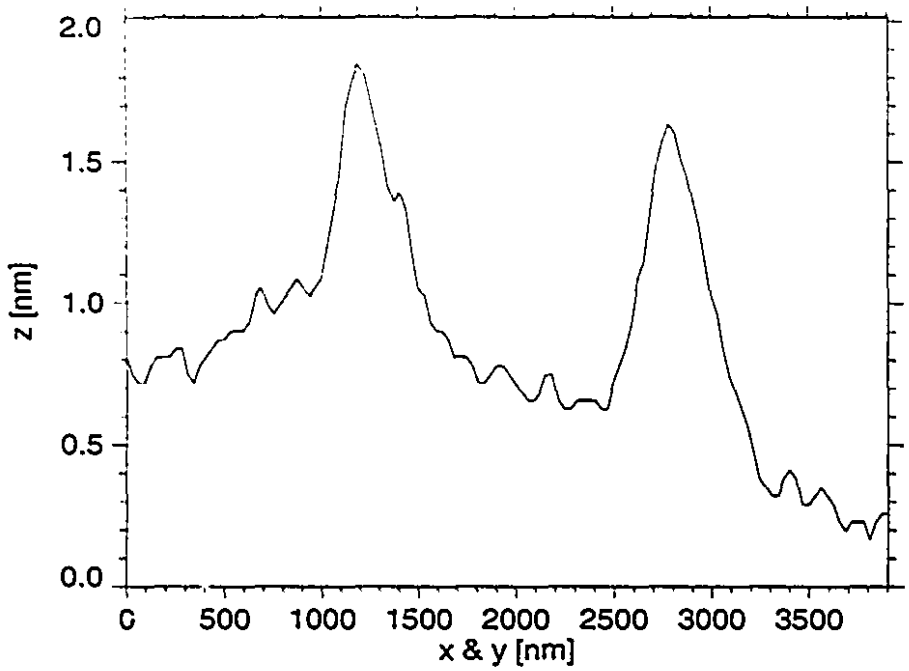

Figure 4.13: Signal profile of the cut through a magnetic domain as shown by the white line in Fig. 4.12 (b). The z-axis represents the intensity of the magnetic signal recorded by the tip.

which are controlled by the alloy composition. Specifically, in the Ni/Co binary alloy system, a maximum of AMR ($\Delta\rho/\rho$) was found at the composition around $Ni_{80}Co_{20}$, which corresponds to a maximum in the initial permeability μ_0, as shown in Fig. 4.14. Furthermore, at this same composition, the magnetocrystalline anisotropy constants and magnetostriction are nearly zero. Since both AMR and magnetostriction involve spin-orbit interactions, theoretically, there is some justification to relate these two quantities; however, there is no experimental evidence to support this relation and, as seen in Fig. 4.14, zero magnetostriction occurs around $x \approx 0.65$, whereas maximum $\Delta\rho/\rho$ actually occurs at $x \approx 0.80$ (Cf. Fig. 1.1). In addition, due to the formation of a common d band[58] between Ni and Co, the room-temperature resistivity of Ni/Co is much lower than other Ni-based alloys, which, therefore, enhances the ratio $\Delta\rho/\rho$. Of technological relevance in magnetic device design, the optimization of maximum magnetoresistance and intrinsic properties is useful in obtaining high magnetic field sensitivity, i.e., an appreciable MR change in unit field.

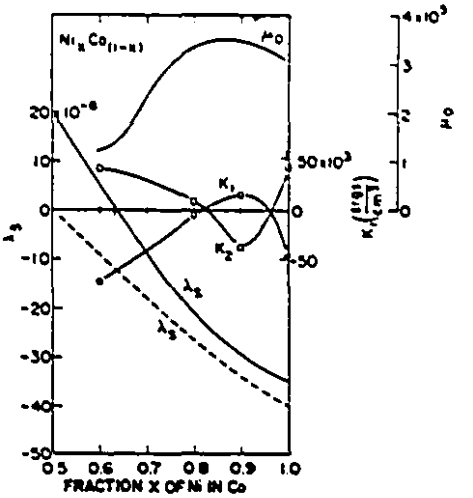

Figure 4.14: Crystalline anisotropy K_1 and K_2, saturation magnetostriction λ_s, and initial permeability μ_0 for Ni_xCo_{1-x}. [After McGuire and Potter, IEEE Trans. Mag. MAG-11, 1018 (1975).]

4.3.1 *Resistivity and Magnetoresistance (MR) of Ni/Co Multilayers*

The magnetoresistivity of the samples was measured at room temperature in the three field orientation described in Chapter 3: (a) field parallel to the current, i.e., longitudinal MR (LMR); (b) field in-plane perpendicular to the current, i.e., transverse MR (TMR); and (c) field perpendicular to the film surface, i.e., perpendicular MR (PMR). Typical MR curves showing the dependence of resistivity on magnetic field are presented in Fig. 4.15. The variation with field depends on the orientation of the applied field. For LMR, the resistance increases at low field, whereas for TMR, the resistance decreases with increasing field. The difference in resistance between the LMR and TMR orientations at saturation field represents the anisotropic magnetoresistance effect. The MR curves in Fig. 4.15 show a full cycle of $\Delta\rho/\rho$ vs. H. The separation of the two peaks in resistivity on either side of the $H = 0$ axis reflects the magnetic hysteresis of the samples. Their positions in fact can be closely correlated to the coercive field H_c in each of the samples (Cf. Table 4.3). Furthermore, it should be noted that the resistivity of the zero-field state depends on the exact domain configuration, so it is also history dependent and is not well defined even for a given sample at a given temperature. The MR curves shown were recorded after one full magnetization cycle.

Table 4.4: Resistivity ρ and magnetoresistive parameters of Ni/Co multilayers. $\Delta\rho = \rho_{\parallel} - \rho_{\perp}$ is defined as the anisotropic magnetoresistivity, the normalized quantity $\Delta\rho/\rho$ is the AMR ratio, H_s is the saturation magnetic field (in-plane), and $(\Delta\rho/\rho)/\Delta H$ is the sensitivity.

Sample	ρ ($\mu\Omega$·cm)	$\Delta\rho$ ($\mu\Omega$·cm)	$\Delta\rho/\rho$ (%)	H_s (Oe)	$(\Delta\rho/\rho)/\Delta H$ (%/Oe)
1000 Å Ni	14.9 ± 0.4	0.15 ± 0.005	1.0	45 ± 5	0.03
500 Å Co	20.7	0.21	1.4	100	0.001
(Ni40Å/Co40Å)×12	19.0	0.34	1.8	60	0.06
(Ni40Å/Co30Å)×12	20.1	0.32	1.6	45	0.06
(Ni40Å/Co20Å)×12	17.9	0.32	1.8	40	0.10
(Ni40Å/Co10Å)×12	17.5	0.42	2.4	85	0.05
(Ni30Å/Co40Å)×12	20.3	0.32	1.6	35	0.06
(Ni20Å/Co40Å)×12	21.2	0.32	1.5	50	0.06
(Ni5Å/Co40Å)×12	33.9				
(Ni40Å/Co5Å)×6	12.3	0.37	3.0	80	0.09
(Ni40Å/Co5Å)×12	14.8	0.36	2.4	85	0.05
(Ni40Å/Co5Å)×24	17.9	0.32	1.8	350	0.004
(Ni40Å/Co5Å)×48	16.3	0.33	2.0	800	0.003

Table 4.4 presents the results of the magnetotransport measurements. The values for $\Delta\rho$ and $\Delta\rho/\rho$ represent the AMR effect described above. The values of $\Delta\rho$ measured for the pure Ni and Co thin films agree closely with the values reported in Table 1.1. The resistivity of the films is nevertheless higher than for the bulk elements, causing a reduction in the AMR ratio $\Delta\rho/\rho$. As can be seen in the Table, $\Delta\rho$ alone is consistently around 0.35 $\mu\Omega$·cm, independent of thickness and composition in all multilayers. Values of the ratio $\Delta\rho/\rho$ depend only on ρ, which therefore deserves closer attention and analysis.

An important consideration in thin film resistivity is size effects. It is well known that resistivity increases as films become thinner due to the additional obstacle for

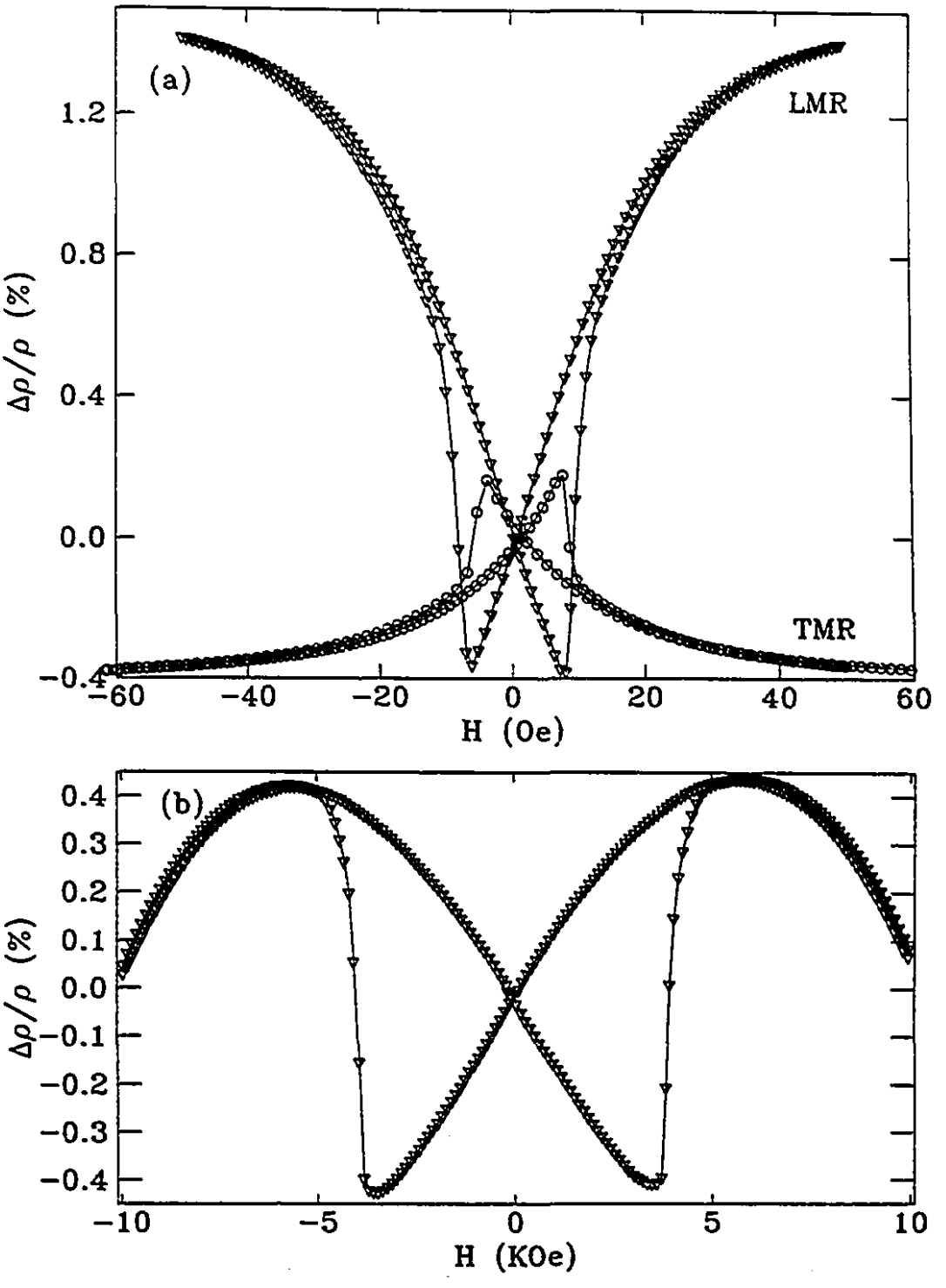

Figure 4.15: Magnetoresistance curves for a Si/(Ni40Å/Co40Å)×12 multilayer with field applied (a) in-plane, longitudinally (LMR) and transversely (TMR), and (b) perpendicular to the plane of the film (PMR).

conduction electrons of diffuse scattering at the surface. For the resistivity to noticeably increase, the mean free path (l) of the conduction electrons must be comparable to the film thickness (t). Under conditions of diffuse scattering, the following approximations have been given by Fuchs[28] and Sondheimer[29]. For a thick film where $l < t$,

$$\rho = \rho_0 \left[1 + \frac{3}{8}(l/t)\right] \tag{4.8}$$

and for a very thin film, where $t \ll l$,

$$\rho = \rho_0 \frac{4(l/t)}{3} \frac{1}{[\ln(l/t) + 0.423]} \tag{4.9}$$

where ρ_0 is the bulk resistivity and ρ is the measured value. The thick film approximation, Eq. 4.8, is a reasonable fit over a wide range of l/t values even when the condition $l < t$ is no longer satisfied. As will be seen below, and from the measured resistivities of roughly 15-20 $\mu\Omega$·cm, a mean free path of 20-30 Å can be estimated. Since the thinnest multilayer has $t = 270$ Å, we may conclude that size effects due to total film thickness are negligible.

In the measurement of thin film resistivity, the effect of grain boundaries must also be considered. Grain boundaries mark the interface of two crystals that have different orientations and thus interrupt the regularity of the lattice. As-deposited thin films may develop a larger number of these grain boundaries than bulk metals, which increases the grain boundary resistivity. No systematic study of the grain structure and size was undertaken in this study. Nevertheless, a clear trend in resistivity for the (Ni40Å/Co5Å)$\times N$ multilayers can be seen in Table 4.4, with resistivity increasing as the number of bilayers N is increased, in correlation with the increased surface roughness as derived from the X-ray structural studies and shown in Table 4.2.

The resistivity of the Si/($\mathrm{Nit_{Ni}}$/$\mathrm{Cot_{Co}}$)$\times$12 multilayers is shown in Fig. 4.16 as well as the theoretical values calculated from Eq. 2.23 which was derived in Chapter 2. The best fit to the experimental resistivities was found by varying the mean free paths, assumed to be symmetric, i.e., independent of θ, the angle between the electron velocity and magnetization vector, for each layer and the transmission coefficient T

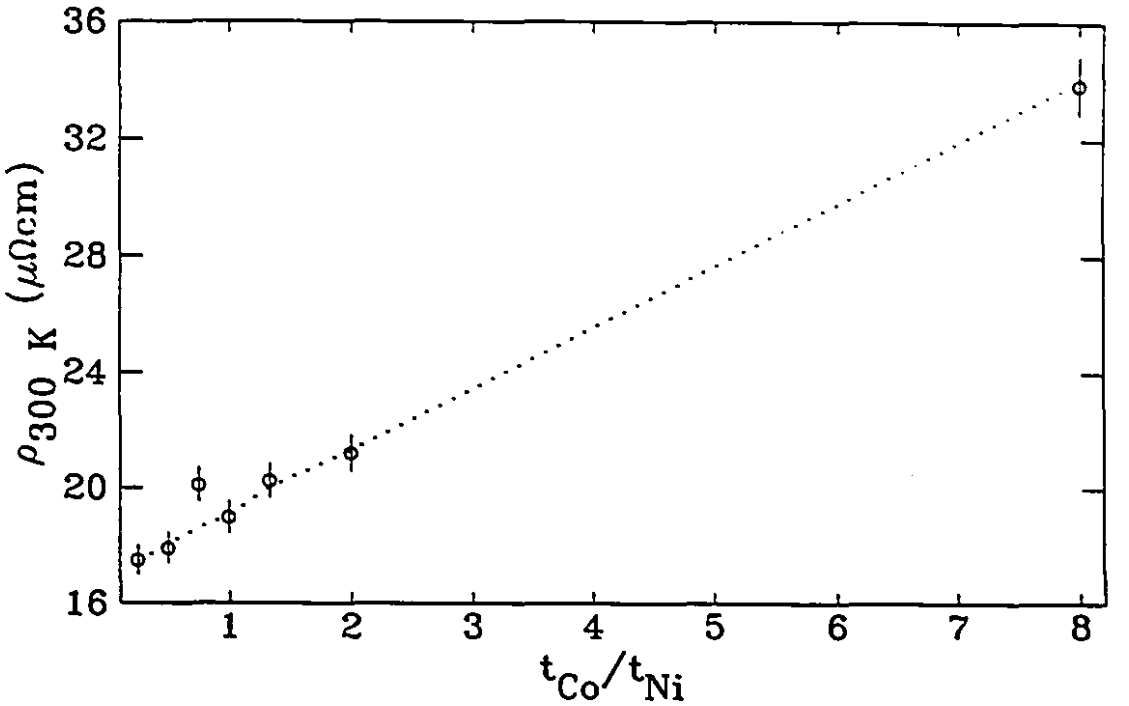

Figure 4.16: Resistivity of Si/(Nit_{Ni}/Cot_{Co})×12 multilayers as a function of the ratio t_{Co}/t_{Ni}. The dotted line is a calculation using the model and parameters described in the text.

from the boundary conditions of Eq. 2.24. The fitted resistivities presented in Fig. 4.16 are calculated with $\lambda_{Ni} = 29.9$ Å, $\lambda_{Co} = 18.9$ Å, and $T = 0.8$. The fit is very sensitive to the choice of this transmission coefficient, which is indicative of the importance of the interface contribution to the resistivity.

Another effect which must be examined in connection with the magnetoresistance of thin films is stress. Residual stresses in films, and in particular evaporated films that are deposited at high temperatures, can be as high as 10^{10} dynes/cm^2 and can be either tensile or compressive. Films deposited at high temperature have a residual stress at room temperature of two kinds. One kind is the thermal stress caused by the difference in thermal contraction of the film and substrate. The second kind is an intrinsic stress resulting from the nucleation and growth of crystallites within the film. In a magnetostrictive material such as nickel, the residual stress may be a strong factor in determining the observed magnetic properties. The response of a film to an applied magnetic field will depend on how the magnetic domains behave when it is stressed,

since it is the magnetization that determines the magnetoresistance. Thus if the hysteresis loop is modified, the observed resistivity as a function of applied field will be correspondingly modified. These changes do not mean, however, that anisotropic magnetoresistance measured under saturation conditions is affected. Based on the effect stress has on the average resistivity of the film, one can speculate that any change in $\Delta\rho$ with stress is probably small. In fact, the large value of magnetostriction for Ni is just a manifestation of the magnetoresistive anisotropic effect, itself caused by stress orientations of the domains. It is estimated[19] that a residual stress of 10^{10} dynes/cm^2 could cause a change in $\Delta\rho/\rho$ of 4×10^{-3}. The change in ρ would be less than 0.5%, and this would have a negligible effect on the AMR ratio.

4.3.2 *Planar Hall Effect (PHE)*

Recall from Eq. 1.3 in the Introduction, the vector form of the electric field E:

$$\mathbf{E} = \rho_\perp(B)\mathbf{J} + [\rho_\parallel(B) - \rho_\perp(B)][\alpha \cdot \mathbf{J}]\alpha + \rho_H(B)\alpha \times \mathbf{J}. \tag{4.10}$$

Referring to Fig. 3.11 in Chapter 3, the current is constrained to flow along the x direction between contacts 1 and 2. For the conventional Hall geometry, the applied field is along z, out of the plane of the film, and the Hall voltage is measured along the y-axis at contacts 3 and 4. However, another effect, called the planar Hall effect, can also give a Hall voltage E_y perpendicular to the current J, in fields which have nothing to do with the Hall effect, i.e., with field applied in-plane. In fact, from Eq. 4.10, we find

$$E_y = (\rho_\parallel - \rho_\perp)\cos\theta \sin\theta J, \tag{4.11}$$

where $\mathbf{J} \cdot \mathbf{M} = \cos\theta$. The PHE is therefore another manifestation of the resistivity anisotropy.

A typical PHE curve on a Si/(Ni40Å/Co10Å)×12 multilayer is shown in Fig. 4.17 for field applied in the longitudinal direction, i.e., parallel to the current. The overall shape of the curve is quite similar to the corresponding MR curves. The most striking feature is the very high value of the ratio $\Delta\rho/\rho$. This high value, however, is an artifact of the initial resistivity, measured transversely to the current, being

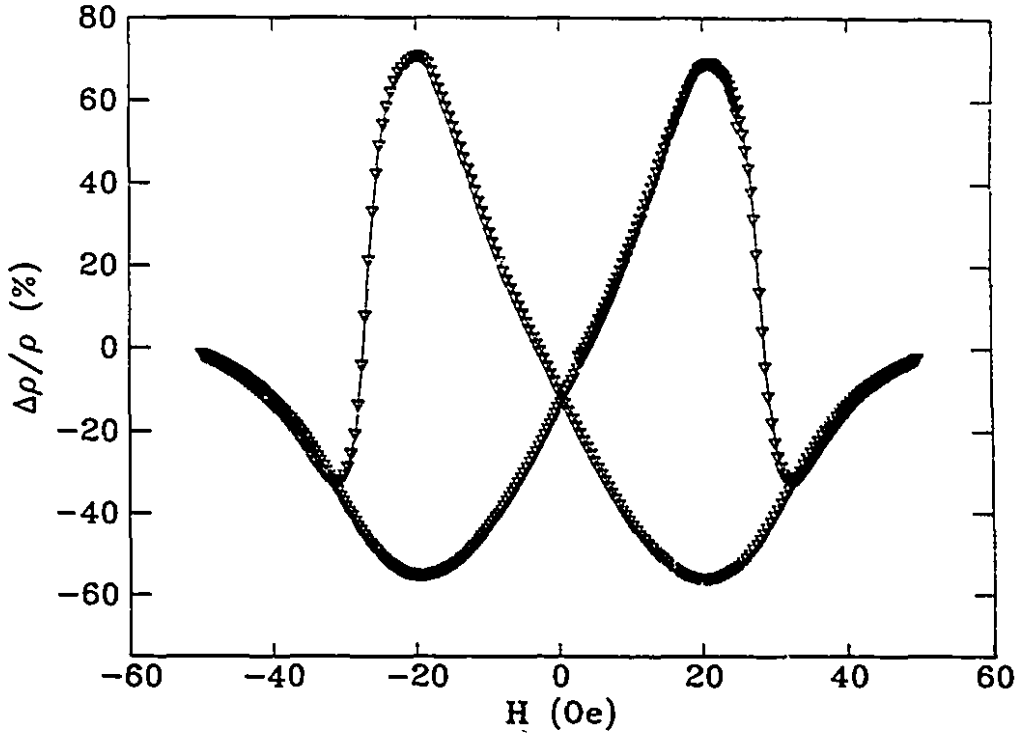

Figure 4.17: Planar Hall effect in a Si/(Ni40Å/Co10Å)x12 multilayer with field applied longitudinally, i.e., parallel to the current.

very small ($\Delta\rho \sim 0.3$ $\mu\Omega$·cm is similar in magnitude to the AMR effect). Since small variations in the positioning of the contacts may radically affect this initial resistance, the ratio $\Delta\rho/\rho$ is not well-defined. Although output signals in a magnetoresistive device are proportional to $\Delta\rho$, the ratio $\Delta\rho/\rho$ is a reasonable figure of merit for device applications because power dissipation is proportional to ρ. For this reason and others, the PHE is being considered for applications in low-field magnetic sensors[59].

4.3.3 *Magnetoresistive Sensitivity*

The primary goal of this thesis was not the refinement of magnetoresistive sensitivity. Nevertheless, the highest sensitivity obtained in the Ni/Co multilayer system, from Table 4.4, was 0.10%/Oe. This value was measured at zero-field, and was constant in the range from ~ -10 Oe to +10 Oe. These sensitivities compare well with current alloys such as Ni-Fe permalloy (sensitivity $\sim$ 0.3 - 0.5%/Oe)[60, 61] used in the fabrication of magnetoresistive devices. Possible improvement of the sensitivity can be

realized. Since $\Delta\rho$ was found to be almost constant in all compositions, an enhanced sensitivity can be achieved by lowering the initial resistivity ρ_0, or by lowering the coercive and saturation fields. The MR data on the series $\mathrm{Si}/(\mathrm{Nit}_{\mathrm{Ni}}/\mathrm{Cot}_{\mathrm{Co}})\times N$, with varying number of bilayers N, indicates that a reduced number of bilayers is desirable in obtaining low saturation fields. The formation of the easy-axis of magnetization in-plane may also be critical for the same purpose. Speculatively, high-temperature deposition or post-deposition annealing of the multilayers may lead to smoother interfaces and reduced resistivity and saturation field. However, this eventual heat treatment must be controlled to prevent total alloying and the disappearance of the superlattice structure.

5

Conclusion

IN THIS THESIS, the structural, magnetic, and magnetotransport properties of sputter-deposited ferromagnetic/ferromagnetic Si/(Nit_{Ni}/Cot_{Co})$\times N$ multilayers were measured. The technological importance of Ni-Co alloys due to their soft magnetic and magnetotransport properties was a motivating factor in the choice of the Ni/Co multilayer system. Also, the influence on magnetotransport properties of layering Ni and Co in a modulated structure was of particular interest. The individual component layer thicknesses, t_{Ni} and t_{Co}, ranged from 40 Å down to 5 Å, and the number of bilayer repetitions N = 6, 12, 24, and 48. The magnetoresistive effect exhibited by these structures, important for magnetic recording and detection devices, has been ascribed to anisotropic magnetoresistance (AMR). A theoretical description of this phenomenon in $3d$ transition metals has been presented.

The main results of this research are as follows:

Structural characterization by grazing-angle X-ray reflectivity indicated a well-defined compositional modulation along the film growth direction. The layer thicknesses extracted from the reflectivity data are within 10% of the nominal values for all multilayer films. The roughness of the individual Ni and Co layers was found to vary between 4.1 Å and 7.9 Å, independent of composition; measured roughness sets an upper-bound on interdiffusion between the multilayers. The roughness of the top surface increases with the number of bilayers N. This has been attributed to the accumulation of small thickness fluctuations associated with each layer. The Ni/Co multilayers are polycrystalline and grow in an FCC phase mostly along the (111) direction, though with a fraction of (200) domains. The multilayer structure is

well-defined and has a long crystalline coherence length of $\sim$ 450 Å.

Multilayers with 12 or less bilayers exhibit a strong in-plane magnetic anisotropy. The origin of the easy-axis of magnetization is not clearly understood, but could be caused by a combination of the residual stress resulting from the mismatch of atomic spacing between the substrate and first Ni layer, and the large negative magnetostriction of Ni. By contrast, multilayers with 24 or more bilayers have no in-plane easy-axis. This result suggests a gradual disappearance of the in-plane easy-axis as the number of bilayers is increased due to relief of the residual stress. The coercivity of the $N = 12$ multilayers varies roughly between 7 and 16 Oe, independent of composition and anisotropy. This variation in coercivity is more likely due to small fluctuations in the deposition conditions and the resultant magnetic domain structure.

The magnetoresistance (MR) of the multilayers is closely correlated to the magnetic hysteresis loops measured by VSM and suggests that anisotropic magnetoresistance (AMR) underlies the effect. The magnitude of the MR $\Delta\rho$ is roughly 0.35 $\mu\Omega$·cm for all multilayers, independent of composition. The ratio $\Delta\rho/\rho$, which is important for devices, depends therefore on the zero-field resistivity ρ and was found to be as high as 3.0% in a Si/(Ni40Å/Co5Å)×6 multilayer. From the compositional variation of resistivity, the elemental layer mean free paths, $\lambda_{Ni} = 29.9$ Å and $\lambda_{Co} = 18.9$ Å, were extracted. These values for the mean free path indicate that size effects due to surface scattering may be neglected, since all multilayers studied had total thicknesses ≥ 270 Å. The transmission coefficient T, which represents the probability of a conduction electron to be transmitted through the interface between two adjacent layers, was equal to 0.8. Moreover, the resistivity was very sensitive to the choice of T, which demonstrates the importance of the interface contribution to the resistivity.

The highest sensitivity $(\Delta\rho/\rho)/\Delta H$ at zero-field was 0.10%/Oe and was constant in the range ~ -10 Oe to $+10$ Oe. This sensitivity compares well with other alloys being developed for magnetic sensors. Even though the primary goal of this thesis was not the refinement of magnetoresistive sensitivity, enhanced sensitivity may be achieved by lowering the initial resistivity ρ or by lowering the coercive and saturation

fields of the multilayers. The MR data for the series of multilayers with varying number of bilayers N indicates that saturation field is smallest in the multilayers with fewer bilayers. The formation of an in-plane easy-axis of magnetization may also be critical in obtaining smaller saturation fields. Furthermore, a study of the effects of high-temperature deposition and post-deposition heat-treatment may lead to an improvement of the MR sensitivity in this multilayer system.

Appendix

A.1 Microscopic Origin of AMR

Here we discuss the microscopic origin of the AMR effect which leads to the anisotropic mean free paths [Eq. 2.18] introduced in the previous section. As was already stated, *sd* scattering is the dominant mechanism in transition-metal conductivity. The ferromagnetic resistance anisotropy must therefore be a consequence of an anisotropic scattering potential. The spin-orbit interaction has been proposed to explain magnetocrystalline anisotropy[62] and resistance anisotropy in ferromagnets[21]. It has the form

$$H_{s.o.} = KL \cdot S \tag{A.1}$$

where L and S are the orbital and spin angular momenta, respectively, and K is the spin-orbit coupling parameter. The spin-orbit interaction contributes, depending on the spin or magnetization direction, to the energy of the d states, making it favorable for the magnetization to point along certain crystallographic directions. Thus the d electron spin is coupled to its orbital motion, which in turn is coupled to the lattice by the crystal field. With M constrained along a particular crystallographic direction, we use quantum mechanics to calculate new wavefunctions ψ_d^1 in terms of the ψ_d^0 that are obtained when the spin-orbit interaction is neglected. The ψ_d^1 exhibit symmetry lower than cubic and are not eigenfunctions of S_z because the spin-orbit interaction mixes states of opposite spin. Therefore, both

$$\frac{1}{\tau_{s\uparrow(\downarrow),d}} \simeq \frac{2\pi}{\hbar} N_d(\epsilon_F) \left| \int \psi^*_{s\uparrow(\downarrow)} V_{\text{scatt}} \psi_d^1 d\tau \right|^2 \tag{A.2}$$

exhibit symmetry lower than cubic. In this equation, $d\tau$ denotes an integration over both spatial and spin coordinates and the k′ dependence of $|V^{sd}_{\mathbf{k},\mathbf{k}'}|^2$ appearing in Eq.

2.11 is ignored for simplicity. A separate spherical parabolic s band is assumed, with

$$\psi_s = e^{i\mathbf{k}\cdot\mathbf{r}}\chi \tag{A.3}$$

where χ is the spin function. Also, $V_{\text{scatt}}(\mathbf{r})$ is assumed to be radial, such that

$$V_{\text{scatt}} = \frac{\Delta Z e^2}{r} e^{-qr} \tag{A.4}$$

where q^{-1} is a screening length. The zero-field conductivity, under these conditions, is

$$\sigma^0_{ij} = \frac{ne^2}{m_s}\frac{3}{4\pi k_F^4}\left[\int \frac{k_i k_j ds}{\frac{1}{\tau_{ss}} + \frac{1}{\tau_{s\uparrow,d}(\mathbf{k})}} + \int \frac{k_i k_j ds}{\frac{1}{\tau_{ss}} + \frac{1}{\tau_{s\downarrow,d}(\mathbf{k})}}\right] \tag{A.5}$$

where k_F is the Fermi wavenumber for s electrons and ds denotes an integration over the spherical Fermi surface in k space.

The zero-field resistivity ρ_0 is assumed to be approximately equal to the resistivity ρ_{av} in the demagnetized state which, using symmetry arguments, can be shown to be approximately

$$\rho_0 \approx \frac{1}{3}\rho_{\parallel} + \frac{2}{3}\rho_{\perp} \tag{A.6}$$

where $\rho_{\parallel}$ and $\rho_{\perp}$ are the resistivities with the magnetization parallel and perpendicular to the current direction, respectively. The results of the calculations for $\tau_{s\uparrow(\downarrow)}$ by Potter[63], when inserted into Eq. A.5, and upon integration[19] yield

$$\frac{\Delta\rho}{\rho_0} = \frac{\rho_{\parallel} - \rho_{\perp}}{\frac{1}{3}\rho_{\parallel} + \frac{2}{3}\rho_{\perp}} = \frac{3(\sigma_{\perp} - \sigma_{\parallel})}{\sigma_{\perp} + 2\sigma_{\parallel}} \tag{A.7}$$

where

$$\sigma_{\parallel} = \sigma_0\left\{1 - \frac{1}{140\beta}\frac{N_d}{N_s}\left[\left(\frac{K}{2\gamma}\right)^2 + \frac{5+2\sqrt{6}}{24}\left(\frac{K}{2\gamma+\epsilon}\right)^2\right] - \frac{3\sqrt{3}\beta}{2}\frac{N_s}{N_d}\ln\left[\frac{1}{16}\left(\frac{K}{\epsilon}\right)^2 + \beta\frac{N_s}{N_d}\right]\right\} \tag{A.8}$$

and

$$\sigma_{\perp} = \sigma_0\left\{1 - \frac{1}{140\beta}\frac{N_d}{N_s}\left[\left(\frac{5}{4}\frac{K}{2\gamma}\right)^2 + \frac{19-2\sqrt{6}}{8}\left(\frac{K}{2\gamma+\epsilon}\right)^2\right] - \frac{3\sqrt{3}\beta}{2}\frac{N_s}{N_d}\ln\left[\frac{1}{32}\left(\frac{K}{\epsilon}\right)^2 + \beta\frac{N_s}{N_d}\right]\right\} \tag{A.9}$$

and

$$\sigma_{\perp} = \sigma_0\left\{1 - \frac{1}{140\beta}\frac{N_d}{N_s}\left[\left(\frac{5}{4}\frac{K}{2\gamma}\right)^2 + \frac{19-2\sqrt{6}}{8}\left(\frac{K}{2\gamma+\epsilon}\right)^2\right] - \frac{3\sqrt{3}\beta}{2}\frac{N_s}{N_d}\ln\left[\frac{1}{32}\left(\frac{K}{\epsilon}\right)^2 + \beta\frac{N_s}{N_d}\right]\right\}. \tag{A.10}$$

The term $\beta(N_s/N_d)$ is due to isotropic *ss* scattering, while ϵ is the energy splitting between the uppermost two *d* bands of like spin at the top of the band, and 2γ is the exchange splitting, assumed uniform, as shown in Fig. 2.1.

BIBLIOGRAPHY

[1] A.L. Greer and F. Spaepen. *Synthetic Modulated Structures.* Academic Press, New York, 1985.

[2] I.K. Schuller. *Physics, Fabrication and Applications of Multilayered Structures.* Plenum Press, New York, 1988.

[3] L.M. Falicov, F. Meija-Lira, and J.L. Moran-Lopez. *Magnetic Properties of Low-Dimensional Systems II.* Springer-Verlag, Berlin, 1990.

[4] L.M. Falicov, D.T. Pierce, S.D. Bader, R. Gronsky, K.B. Hathaway, H.J. Hopster, D.N. Lambeth, S.S.P. Parkin, G. Prinz, M. Salamon, I.K. Schuller, and R.H. Victora. *J. Mater. Res.*, 5:1299, 1990.

[5] S.S.P. Parkin. Research report. Technical report, IBM Research Division, Almaden Research Center, 1993.

[6] C.J. Robinson, T. Suzuki, and C.M. Falco, editors. *Magneto-Optic Data Storage*, Pittsburgh, 1989. Mater. Res. Soc. Symp., Vol. 150.

[7] F.J.A. den Broeder, W. Hoving, and P.J.H. Bloemen. *J. Magn. Magn. Mater*, 93:652, 1991.

[8] M.N. Baibich, J.M. Broto, A. Fert, F. Nguyen van Dau, F. Petroff, P.E. Etienne, G. Creuzet, A. Friederich, and J. Chazelas. *Phys. Rev. Lett.*, 61(2472), 1988.

[9] P. Gruenberg, R. Schreiber, Y. Pang, M.N. Brodsky, and H. Sowers. *Phys. Rev. Lett.*, 57:2442, 1986.

[10] S.S.P. Parkin, N. More, and K.P. Roche. *Phys. Rev. Lett.*, 64:2304, 1990.

[11] D. Neerinck, K. Temst, M. Baert, E. Osquiguil, C. van Haesendonck, Y. Bruynseraede, A. Gliabert, and I.K. Schuller. *Phys. Rev. Lett.*, 67:2577, 1991.

[12] I.K. Schuller, A. Fartash, E.E. Fullerton, and M. Grimsditch. Thin films: Stresses and mechanical properties III. page 499, Pittsburgh, 1992. Mater. Res. Soc., Vol. 239.

[13] J.M. Gallego, D. Lederman, T.J. Moran, and I.K. Schuller. *Appl. Phys. Lett.*, 64:2590, 1994.

[14] J.M. Freitag, X. Bian, Z. Altounian, J.O. Ström-Olsen, and R.W. Cochrane. page 359. Mater. Res. Soc. Symp. Proc., Vol. 384, 1995.

[15] A.B. Pippard. *Magnetoresistance in Metals.* Cambridge University Press, Cambridge, 1989.

[16] M. Olivier. PhD thesis, McGill University, Montreal, November 1984.

[17] L. Berger. *J. Appl. Phys.*, 49:2156, 1978.

[18] I.A. Campbell and A. Fert. *Ferromagnetic Materials*, volume 3, chapter 9. North-Holland Publishing Company, 1982.

[19] T.R. McGuire and R.I. Potter. *IEEE Trans. Magn.*, MAG-11(4):1018, 1975.

[20] T. Farrell and D. Greig. *J. Phys. C*, 1:1359, 1968.

[21] J. Smit. *Physica*, XVI(6):612, 1951.

[22] H.C. van Elst. *Physica*, 25:708, 1959.

[23] N.W. Ashcroft and N.D. Mermin. *Solid State Physics*, page 6. W. B. Saunders Company, 1976.

[24] A.C. Smith and J.F. Janak. *Electronic Conduction in Solids*, page 192. McGraw-Hill Inc., 1967.

[25] N.F. Mott. *Proc. R. Soc. London Ser. A*, 153, 1936.

[26] N.F. Mott. *Proc. R. Soc. London Ser. A*, 156, 1936.

[27] Th. G. S. M. Rijks, R. Coehoorn, M. J. M. de Jong, and W. J. M. de Jonge. *Physical Review B*, 51:283, 1995.

[28] K. Fuchs. *Proc. Cambridge Philos. Soc.*, 34:100, 1938.

[29] E.H. Sondheimer. *Philos. Mag. Suppl.*, 1(1):1, 1952.

[30] R. Q. Hood and L. M. Falicov. *Physical Review B*, 46:8287, 1992.

[31] B. Dieny. *J. Phys. Condens. Matter*, 4:8009, 1992.

[32] R. Weil and R.G. Barradas, editors. *Electrocrystallization.* The Electrochemical Society, Pennigton, 1981.

[33] J.L. Vossen and W. Kern, editors. *Thin Film Processes.* Academic Press, New York, 1978.

[34] J.L. Vossen and W. Kern, editors. *Thin Film Processes II.* Academic Press, Boston, 1991.

[35] M. Ohring. *The Materials Science of Thin Films.* Academic Press, Boston, 1992.

[36] E.W. Williams. *J. Magn. Magn. Mater.*, 95, 1991.

[37] K.E. Meyer, I.K. Schuller, and C.M. Falco. *J. Appl. Phys.*, 52, 1981.

[38] Planar magnetron sputter source manual. Technical report, ION Tech Limited, 1989.

[39] Simon Foner. *Rev. Sci. Instr.*, 30, 1959.

[40] P.N. Argyres. *Phys. Rev.*, 97, 1955.

[41] S.D. Bader. *J. Magn. Magn. Mater.*, 100, 1991.

[42] R.W. Cochrane, B.J. Kastner, and W.B. Muir. *J. Phys. E*, 15, 1982.

[43] W.B. Muir and J.O. Ström-Olsen. *J. Phys. E*, 9, 1976.

[44] E.E. Fullerton, I.K. Schuller, and Y. Bruynseraede. *MRS-Bulletin*, page 33, December 1992.

[45] E.E. Fullerton, I.K. Schuller, H. Vanderstraeten, and Y. Bruynseraede. *Phys. Rev. B*, 45:9292, 1992.

[46] M. Born and E. Wolf. *Principles of Optics.* Pergamon Press, Oxford, 1964.

[47] Y. Huai, M. Chaker, J.N. Broughton, E. Gat, Pépin, T. Gu, X. Bian, and M. Sutton. *Appl. Phys. Lett.*, 65:830, 1994.

[48] B.K. Agarwal. *X-ray Spectroscopy.* Springer, Berlin, 1979.

[49] Y. Huai. PhD thesis, Université Montréal, November 1992.

[50] T. Gu. PhD thesis, McGill University, March 1994.

[51] Y. Huai, R.W. Cochrane, and M. Sutton. *Phys. Rev. B*, 48:2568, 1993.

[52] X. Bian. PhD thesis, McGill University, August 1994.

[53] F.J. Lamelas, H.D. He, and R. Clarke. *Phys. Rev. B*, 43:12296, 1991.

[54] A.P. Payne and B.M. Clemens. *Phys. Rev. B*, 47:2289, 1993.

[55] M. Cai, T. Veres amd R. Morel, and R.W. Cochrane. *J. Appl. Phys.*, 79:6289, 1996.

[56] G.H.O. Daalderop, P.J. Kelly, and F.J.A. den Broeder. *Phys. Rev. Lett.*, 68:682, 1992.

[57] P. Grütter, H.J. Mamin, and D. Rugar. Magnetic force microscopy. In R. Wiesendanger and H.-J. Guentherodt, editors, *Springer Series in Surface Science 28. Scanning Tunneling Miscroscopy II*, pages 151–207. Springer, Berlin, 1992 a.

[58] T.R. McGuire, W.D. Grobman, and D.E. Eastman. *AIP Conf. Proc.*, 18:903, 1973.

[59] A. Schuhl, F. Nguyen Van Dau, and J.R. Childress. *Appl. Phys. Lett.*, 66:2751, 1995.

[60] P. Ciureanu, G. Rudkowska, P. Rudkowski, and J.O. Ström-Olsen. *IEEE Trans. Magn.*, MAG-29:2251, 1993.

[61] T. Miyazaki, T. Ajima, and F. Sato. *J. Magn. Magn. Mater.*, 81:86, 1989.

[62] H. Brooks. *Phys. Rev*, 58:909, 1940.

[63] R. I. Potter. *Phys. Rev. B*, 10:4626, 1974.